Physics – Uspekhi **62** (12) 1214 – 1232 (2019)

INSTRUMENTS AND METHODS OF INVESTIGATION PACS numbers: 07.57.Pt, **87.61. – c**

Ultrahigh field magnetic resonance imaging: new frontiers and possibilities in human imaging

M A Zubkov, A E Andreychenko, E I Kretov, G A Solomakha, I V Melchakova, V A Fokin, C R Simovski, P A Belov, A P Slobozhanyuk

DOI: https://doi.org/10.3367/UFNe.2018.12.038505

Contents

Abstract. Increasing the strength of the static magnetic field is the main trend in modern magnetic resonance imaging (MRI) of humans. Performing MRI in ultrahigh fields (7 T or more) involves many effects both enhancing and diminishing the image quality, and some effects previously unobservable in weaker fields. We review the main impacts of using ultrahigh fields in human MRI, including new challenges and the solutions proposed. We also discuss new magnetic-resonance scan methods that were unavailable with lower field strength (below 7 T).

Keywords: magnetic resonance imaging, metamaterials, NMR spectroscopy, image processing

M A Zubkov [1], **A E Andreychenko** [1], **E I Kretov** [1], **G A Solomakha** [1], **I V Melchakova** [1], **V A Fokin** [2], **C R Simovski** [1,3], **P A Belov** [1], **A P Slobozhanyuk** [1]

[1] St. Petersburg National Research University of Information Technologies, Mechanics and Optics (ITMO), Kronverkskii prosp. 49, 197101 St. Petersburg, Russian Federation

[2] Almazov National Medical Research Centre of the Ministry of Health of the Russian Federation, ul. Akkuratova 2, 197341 St. Petersburg, Russian Federation

[3] School of Electrical Engineering, Aalto University, PO Box 11000, Aalto, FI-00076, Finland

E-mail: m.zubkov@metalab.ifmo.ru

Received 31 August 2018, revised 18 December 2018
Uspekhi Fizicheskikh Nauk **189** (12) 1293 – 1314 (2019)
DOI: https://doi.org/10.3367/UFNr.2018.12.038505
Translated by Yu V Morozov; edited by V L Derbov

1. Introduction

Magnetic resonance imaging (MRI) is a method for studying the internal structure of various objects by recording nuclear magnetic resonance (NMR) signals from these objects in a magnetic field with specially formed heterogeneity. MRI has a history of more than half a century in Russia [1] and a slightly shorter one abroad [2]. New theoretical insights and technologies gradually change the landscape of MRI as a field of expertise by generating new principles of obtaining magnetic resonance (MR) images (called tomograms in Russia) that open up new areas for MRI application and improve approaches to the analysis of images. The main trend in modern human magnetic resonance imaging has always been to transfer clinical MR studies from weak magnetic fields which are termed low magnetic fields among MRI specialists (up to 1 T) to the so-called high (1–3 T) and, recently, ultrahigh (over 3 T) magnetic fields.

The spectrum of clinical MR studies has been markedly extended due to the transition from low-field to high-field technologies. Using high magnetic fields in human MR imaging made it possible to improve the time resolution of the method, reduce the duration of examination, and thereby facilitate MR visualization of moving organs, such as the heart, liver, and bowels. It has enabled physicians to examine the liver and other parenchymal organs within a single breath hold with high spatial resolution and improved soft tissue contrast, which is of special importance for diagnosing cancer [3]. The enhancement of temporal resolution made possible morphological and functional diagnostic studies of the heart requiring rapid visualization in different phases of the cardiac cycle [4]. The cardiac function is evaluated numerically by

measuring the ejection fraction, i.e., the volume and percentage of blood leaving the heart each time it contracts or per unit time. Moreover, high field MRI affords a unique opportunity to use paramagnetic contrast agents to assess myocardial blood flow using the dynamic MR perfusion technique [5], which is equally extensively employed to evaluate blood supply to the brain [6]. High field MRI (especially in a 3 T field) makes it possible to study perfusion without the application of contrast agents, simply by tagging inflowing blood in neck vessels with radiofrequency label and calculating the blood flow rate in cerebral tissues [6]. This arterial spin labeling (ASL) method has been extensively applied in the diagnostics of various neurologic and psychiatric disorders due to its noninvasive nature and the absence of radiation exposure. Limitations on the frequency of such MR studies are generally less rigorous than for analogous studies with the use of ionizing radiation.

Only the advent of ultrahigh field MRI opened up prospects for the application of such new methods for investigating physiological processes in the brain as functional MRI (fMRI), MR morphometry, and visualization of neural pathways (MR tractography). Functional MRI employing the blood oxygenation level-dependent (BOLD) contrast effect allows identifying functional activity areas in the cerebral cortex under external stimuli or at rest through characterizing the relationships between various brain regions [7]. MR morphometry is a method making use of semi-automatic segmentation and the calculation of the volume of various brain structures [8]; it allows differentiation between neurologic disorders including various forms of dementia, such as Alzheimer's disease and vascular dementia. MR tractography allows determining the principal direction of water transport in neural pathways (i.e., along myelin sheath of the pathway) based on results of so-called Diffusion Tensor Imaging (DTI) [9] and thus visualizing nerve fibers in the brain and other organs; the method finds applications in clinical neuro-oncology as well as in basic neurophysiological research.

MR spectroscopy using nuclei of hydrogen, phosphorus, and other elements is worth to be mentioned separately as a method for noninvasive diagnostics at the biochemical level, since it allows determining levels of choline as a marker of cellular membrane integrity, lactate (marker of anaerobic glycolysis and indicator of tissue hypoxia), N-acetylaspartate (marker of neuronal activity), and some other metabolites [10]. Phosphorus ultrahigh field MR spectroscopy is used to characterize energy processes in the liver and muscles by measuring adenosine triphosphate (ATP) and adenosine diphosphate (ADP) levels [11,12].

The development of ultrahigh field MRI greatly contributed to noninvasive visualization of vessels via phase-contrast techniques, in which moving blood serves as a natural contrast medium. Such studies in high magnetic fields make possible four-dimensional (4D) visualization of the blood flow (either laminar or turbulent) for planning cardiovascular interventions [13]. The use of ultrahigh field MRI for evaluating musculoskeletal disorders resulted in the robust visualization of the cartilage structure and detection of its degenerative changes before their visible manifestation [14].

In other words, the use of high-field MRI in clinical practice has not only improved anatomical visualization of different parts of the human body but also facilitated the assessment of physiological and even biochemical processes in the body without detrimental effects from the application of 3 T magnetic fields. Ultrahigh field MRI opens up even greater prospects. Some authors question the practicability of further increases in magnetic field induction in MRI [15]. Nevertheless, we believe it is worthwhile and even inevitable to move to clinical and pre-clinical MRI studies in ultrahigh fields, bearing in mind the numerous advantages of such an approach over high-field MRI. Some of them are easy to account for by considering the principles of MR imaging, while others arise due to the dependence of the object of interest properties on the magnetic field strength. Certainly, ultrahigh field technologies are not devoid of drawbacks giving rise to criticism [15]. Both the advantages and disadvantages of ultrahigh field technologies are discussed in Section 2. Since this paper is intended for a wide community of physicists, including those unfamiliar with MRI, a discussion of the features of ultrahigh-field MRI is possible only after a brief presentation of the basic principles of MRI as one of the methods of experimental physics.

2. Features of ultrahigh field magnetic resonance imaging

In principle, MRI is a special case of NMR spectroscopy. It is well known that atomic nuclei with a nonzero spin undergo Zeeman splitting of energy levels in a static magnetic field. For example, there are two levels for the spin 1/2 of a proton entering a water molecule (hydrogen is present in water molecules in the form of two protons). The difference between the energies of the upper and lower levels is proportional to the static field magnitude B_0. The application of a radiofrequency (RF) magnetic field to an object containing water or another substance having atomic nuclei with a nonzero spin gives rise to nonequilibrium resonant quantum transitions if the field frequency equals the nuclear precession frequency (Larmor frequency). Such an RF field is created at the Larmor frequency by transmitting antennas called coils in MRI, even if the antenna system is an array of dipole antennas. This term needs clarification. While the magnetic and electric field strengths are equal in the far-field radiation zone of the antenna system up to the free space wave impedance factor, the magnetic field of the antenna in the near-field zone can prevail over the electric field. Since the distance between the object and the antenna system in MRI is shorter than the wavelength and the electric RF field of the antenna is a parasitic effect (i.e., it produces no useful signal and causes only induction heating of biological tissues), antenna systems in MRI are intended only to generate a magnetic near field. In this context, the use of the term RF coil in MRI is fully justified.

Thus, the primary magnetic field of the Larmor frequency generated by an RF coil causes excitation of the upper Zeeman state of atomic nuclei in the object followed by a return to the lower state, the recovery of the equilibrium state being accompanied by the emission of secondary radiation with the same carrier frequency. The interaction of this radiation with either separate RF receiver coils or the same transceiver coils (which is possible owing to time delay relative to the primary RF pulse) provides a basis for the appearance of the NMR signal being recorded [16]. A specific feature of MRI as a variant of NMR spectroscopy is the purposeful generation of a temporary static magnetic field with strength varying in different parts of the studied object (usually, with linear spatial nonuniformity). For this purpose,

DC pulses (so-called gradient pulses) are applied to special direct current coils (*gradient coils*) arranged around the perimeter of the MRI scanner bore. Due to the nonuniformity of the static field, the NMR signal excited in the RF receiver coil by radiation from different parts of the object differ not only in amplitude (because of different concentrations of atomic nuclei of the given substance in different parts of the object) but also in frequency. This allows relating the amplitude of the NMR signal of a given frequency to the coordinates of the respective region inside the object, giving a picture of the spatial distribution of the mass density of the studied substance, e.g., water, fats, or phosphorus, in the object [7, 17]. Additional analysis of phase relationships among several NMR signals recorded after the application of a given sequence of RF pulses and gradient pulses [7, 17] provides detailed MR images of different object cross sections, but the description of such details of the method (even if essential ones) is beyond the scope of the present review.

It is important for further consideration to note that NMR has the following characteristics due to the quantum nature of the effect: limited frequency band and proportionality of the frequency of the observed signal to the magnitude of the static magnetic field induction B_0. Despite its quantum nature, the NMR phenomenon can in the majority of cases be described in classical terms as the RF field-induced precession of macroscopic nuclear magnetization around a static magnetic field. According to this model, the influence of the RF field leads to the deflection of the macroscopic magnetization vector from the equilibrium direction, i.e., the direction of the static magnetic field. It is clear in the above context that the alternating Larmor frequency RF field should have the direction of the magnetic vector differing from that of the static one if NMR is to be observed. For the maximally efficient interaction with the precessing macroscopic nuclear magnetization vector, the RF field (denoted in MRI by B_1^+) must be circularly polarized in the plane orthogonal to the $\mathbf{B}_0$ vector. In such a case, NMR is usually described by the equations for forced precession of the magnetic moment in a stationary or rotating coordinate system (Bloch equations). These equations provide a semi-classical model of the effect in question. The Bloch equations can be supplemented if appropriate by relaxation, gradient, or diffusion terms, depending on the described experiment [7–9, 17].

On the other hand, the resonance frequency of most isotopes with a nonzero magnetic moment in the currently highest possible magnetic fields falls into the RF range. This means that MRI can be regarded as a branch of radiophysics. From this standpoint, NMR spectroscopy and MRI can be considered to be two sequential issues, one being the creation of a uniform RF magnetic field in a given region, the other the reception, amplification, and registration of a weak narrowband signal in the near field of one or several coils. In this case, receiving coils can be either coincident with or different from transmitting ones. The magnitude of magnetic field induction does not directly affect radiotechnical components of the NMR equipment, but its influence on the operating frequency of the spectrometer or scanner RF system makes the parameters of RF energy reception and transmission depend on the strength of the static magnetic field in which NMR is observed. Specifically, a usual consequence of an increase in a constant magnetic field is the quadratic increase in the NMR signal amplitude and, as a result, in MRI sensitivity [17]. Due to this, ultrahigh field MRI provides high-quality images unobtainable by high-field technologies. In other words, ultrahigh field MRI opens up new possibilities for experimental studies of the brain, internal organs, joints, and the nervous and other systems of the human body.

However, detailed analysis of MRI from the radiotechnical standpoint indicates that increasing the constant magnetic field B_0 to 3 T or higher has negative consequences, such as heating of the patient's body or a biological tissue sample [18] and greater spatial nonuniformity of the RF magnetic field [19]. Both effects are due to a rise in the frequency of the observed NMR signal proportional to B_0. The enhanced spatial nonuniformity is a natural result of the accompanying decrease in the operational wavelength in magnetic fields higher than 3 T. Although the size of a body part or a tissue sample being investigated is, as a rule, smaller than the electromagnetic field wavelength in free space, it is often greater than the wavelength inside the body (in high-field and especially ultrahigh-field MRI technologies). It can be accounted for by the fact that biological tissue contains a large amount of water characterized at radiofrequencies by a high refractive index (i.e., the length of a refracted wave inside the tissue markedly decreases). As a result, internally reflected waves interfere inside the body (in other words, a standing wave forms). The electromagnetic field in a standing wave is known to be strongly nonuniform due to an alternating pattern of nodes and antinodes. The scale of characteristic field nonuniformity decreases as B_0 grows and the wavelength shortens. When the RF field nonuniformity scale happens to be comparable to the size of the structures being visualized in the study sample, their images undergo deformation. Thus, the two central radiotechnical problems in ultrahigh field MRI are nonuniformity of the primary (and secondary) RF field arising from the interference of electromagnetic radiation inside the object of study and enhanced absorption of RF energy by the object, resulting in its heating [15, 20, 21].

From the point of view of the relaxation theory, the simplest NMR experiment is characterized by disturbed equilibrium particle distribution over energy levels with subsequent recovery of the initial state after the end of the RF pulse and (partly) during the pulse. In this case, the strength of the static magnetic field directly affects the energy exchange rate between spins and between the spins and the environment. In MRI, the energy exchange rate is characterized by constants T_1, T_2 (spin-lattice and spin-spin relaxation times, respectively), and T_2^* also including the influence of the surrounding medium (at a microscopic scale) on transverse nuclear magnetization. The dependences of T_1, T_2, and T_2^* on B_0 are ambiguous and depend on the properties of the studied substance. In the context of clinical MRI, they are responsible first and foremost for the change of the difference between signals (contrast) from selected tissues or the altered duration of the experiment due to a change in the time of return of macroscopic magnetization to the initial state [22]. The difference in T_1 provides a basis for new diagnostic modalities of ultrahigh field MRI inaccessible with low- and even high-field technologies [23].

However, difficulties arising from RF field nonuniformity necessitate the development of novel scanning methods for correct visualization of relaxation time T_1 distribution in the anatomical region of interest without exceeding the permissible RF radiation exposure levels for a given patient [24, 25]. A rise in T_1 and increased risk of heating the patient's body prevent correct T_2-weighting by classical MR scan methods. Therefore, new methods for

obtaining T_2-weighted images are being developed for the purpose of ultrahigh field MRI [26–28]. Changes in T_2^* contrast markedly affect functional magnetic resonance imaging (fMRI) as a whole (see Section 6).

Even such a brief review of ultrahigh field MRI studies shows that a rise in B_0 is an important though nontrivial step in modern MR studies. It opens up new prospects for MRI application and the development of novel MR-scanning techniques; sometimes, it leads to a change in the clinical MR research paradigm.

The present article is designed to overview the most important practical and technical solutions and innovations relevant to MRI driven by the advent of ultrahigh-field MR scanners for obtaining human body scans. To recall, ultrahigh-field scanners of a smaller size have already proven to be effective tools for scanning laboratory animals and observing various processes in living organisms. The extent of research in magnetic fields higher than 3 T using laboratory animals is much greater than that of analogous human studies, one reason being the limitation imposed on the application of ultrahigh-field scanners in clinical studies that are currently allowed only in a few countries with the use of a single specifically designed tomographic system. Pre-clinical tomographic studies will be briefly mentioned below on account of the possibility of employing certain pre-clinical tomography methods in clinical MRI, but no detailed review of these studies is presented in this paper due to space restrictions.

3. Volume and multichannel transmit/receive systems

Annular resonators coaxial with the MRI tunnel serve as traditional volume RF coils for the spin excitation. Most frequently used in low-field (lower than 1.5 T) and high-field (1.5–3 T) MRI technologies are birdcage [29] and TEM [1] resonators [30]. In these volume coils, an electric current flows in conductors along the tunnel axis, while a standing wave is generated in azimuthal directions. When the coil geometric size is limited by the tunnel size, a significant slowdown of the standing wave is needed to ensure coincidence of its length and the NMR signal wavelength; this is achieved by the use of either large-value capacitors [29] or capacitance between the concentric layers of wires [30]. Both resonators create a maximally uniform (at least in the absence of an object) primary RF field inside the coil. If the object of study centers on the coil axis, the RF field in its center is rather high and corresponds to the standing wave antinode that appears due to internal reflection of the field in the object (see Section 2). Nodes of a standing wave are spaced approximately a quarter wavelength away from antinodes. At frequencies below 130 MHz, corresponding to constant magnetic fields of 3 T or lower, the wavelength in tissues with typical permittivity $\varepsilon_r \approx 50-60$ [31] is relatively large compared, for instance, with the size of the human brain. In such a case, no standing wave nodes appear inside the volume being scanned. At a constant 7-T field level (corresponding to an operational frequency of ~ 300 MHz), the wavelength in the human brain is on the order of 13 cm; in other words, it becomes comparable with the scan area, which leads to the scanning artifacts on the MR image. Therefore, conventional RF coils are believed to be inefficient for the purpose of ultrahigh field MRI. It is still unclear how big the influence of tissue dielectric permittivity on field B_1^+ uniformity is [32]. There is one more factor affecting B_1^+ field inhomogeneity, namely, the high electrical conductivity of biological tissues, which is difficult to measure and can depend on a number of factors that are not easy to define or take into consideration. High electrical conductivity is responsible for the reduced influence of dielectric effects, which make the field B_1^+ distributions more uniform [33]. Improving homogeneity of magnetic field distribution inside the object of study remains a key problem in ultrahigh field MRI.

Creating a more uniform RF field in an ultrahigh field MRI system (compared with the field generated by conventional volume coils) is possible if the coil is a set of antenna elements in which the signal phase and amplitude for each conductor are controlled on an individual basis and optimized taking into account the properties of the object. The process of optimization of the phase and the amplitude of a signal fed to individual coils is called RF shimming [34, 35]. It is performed by measurements of the spatial distribution of the field generated by individual coil elements, with subsequent calculation (using the distributions thus obtained) of the necessary set of signal phases and amplitudes to ensure maximum field uniformity in the selected region. Something like this is realized on a clinical level in volume birdcage [29] and TEM [30] coils. Considering any of them to be a resonator leads to the conclusion that each has two linearly polarized eigenmodes that can be excited with a 90° phase shift, which corresponds to the circular polarization of the RF magnetic field inside the coil. However, using two independent supply channels allows these two modes to be excited with any other phase difference. The choice of the phase difference of other than 90° can be used to compensate for the deviation of field polarization from the circular one induced by the object; as a result, the object's spin system will be excited by the field with polarization maximally close to the circular one, and image quality will be improved. Such phase optimization represents RF shimming of the simplest type used in modern scanners with a magnetic field induction of 3 T for examining human thoracic and abdominal cavities [36]. However, RF shimming with the use of two signal channels is insufficient to study the brain and deeply located organs in the human body. To reduce RF field inhomogeneity in such a case, it is necessary to increase the number of channels. The process of spin system excitation by many independent signal channels is called parallel transmission [37]. The overall distribution of the RF field in a multichannel coil consisting of independently fed antenna elements can be made essentially more uniform than that of the field of a similarly sized double-channel coil.

In the construction of such multichannel coils (in fact, antenna arrays with amplitude and phase distributions), decoupling of antenna elements becomes a pressing challenge. The mutual coupling of elements in such devices are very strong, because the distances between the neighboring wires are 10 or more times shorter than the wavelength. Unlike the interaction of elements in a conventional array antenna, the interaction between elements of such a coil not only leads to array detuning and the distortion of its directional pattern (of little significance for MRI) but also makes shimming impossible. It requires optimization of current phase and amplitude in the array from real signal sources with specially chosen amplitude and phase. The most adequate model of coil element feeding is a voltage generator with finite (known) output impedance. Cross-coupling of

[1] TEM — transverse electromagnetic.

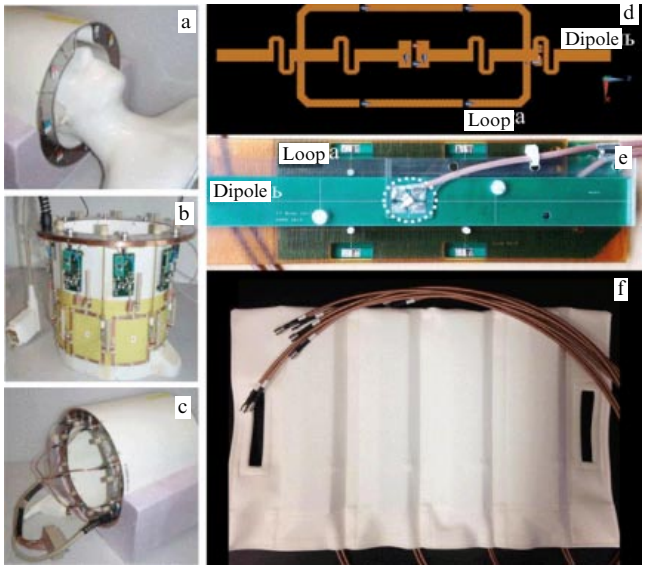

Figure 1. (Color online.) (a–c) Eight-channel RF coil for human brain studies. (d, e) Element of a 16-channel coil based on a combination of dipoles and loops for human body investigation in a 7-T field. (f) Upper part of the 16-channel coil based on a combination of dipoles and loops for human body investigation.

elements that is too strong results in the relationship between currents in coil elements and voltages applied to them becoming virtually unpredictable, which makes controlling the current in them impossible. For this reason, the use of antenna arrays for RF shimming implies the necessity of reducing cross-coupling to an acceptable level.

Currently, ultrahigh-field MRI uses loop antenna arrays [38], resonant section of transmission lines [39], and dipole antennas [40] as antenna elements of coils operating in parallel transmission mode. The best option is to use loop antenna arrays [41] for brain studies in 7-T and higher fields (Fig. 1a–c) and a combination of dipoles and loop antennas for imaging the whole human body [42] (Fig. 1d–f).

Decoupling of RF coil array elements is a subject of extensive research. The main reasons of cross-coupling between loop antennas are mutual inductance and resistive coupling through the study object. Mutual inductance of two loops may have both positive and negative consequences. This property is used in the most popular loop decoupling technique based on the partial overlap of neighboring elements. The correct choice of the overlap region ensures cancellation of mutual inductances of overlapping and nonoverlapping parts of two loops [43]. Sometimes, additional passive loops are used to improve the decoupling [44]. One of the widely known loop decoupling methods is based on capacitors [45] simultaneously included in loop shoulders; another is transformer decoupling [46]. Decoupling techniques for RF coils arranged in the form of electric dipole arrays remain to be improved. One approach to solving this problem is the placement of a passive dipole between its two active neighbors [47]. The main disadvantage of this method is the strong influence of the passive dipole on field distribution in the human body. In another technique for decoupling dipole antennas spaced roughly $\lambda/10$ apart [48], decoupling is achieved by positioning the antenna array on the surface of the structure (representing a two-dimensional analog of photonic crystals), so that the coil operating frequency falls within the structure's band gap [49].

In the case of parallel transmission, superposition of the fields of antenna elements occurs either in the so-called static regime (when the relationship between the currents in coil signal channels of the antenna array remains unaltered during emission of RF pulses) or in the dynamic regime. In the latter case, signals from individual channels vary from pulse to pulse, which allows reaching high spatial homogeneity of the angular deviation of the macroscopic nuclear magnetization direction. The homogeneity is achieved owing to multiple excitations by short pulses at small deflection angles (i.e., at low RF field amplitudes) with different contributions from the channels during the emission of individual pulses [50]. The static regime of parallel transmission is largely used for ultrahigh field imaging of the brain [41, 51, 52], heart [53–55], and other organs [56–60]. In the dynamic regime [61], each low-amplitude RF pulse [61] serves to extract information from some part of the space, either physical (with a spatial region being highlighted by means of channel weighting redistribution) or phase. In the latter case, pulses of magnetic field gradients turned on during intervals between RF pulses are used to distinguish a region in the wave vector space. Such an approach provides many more degrees of freedom to control RF field uniformity. In the dynamic regime, each additional excitation ensures better overall homogeneity of the final image than static parallel transmission [62–64]. To recall, optimization is needed not only for maximum homogeneity of the magnetization deflection angle in a given spatial region but also to reduce the risk of patient overheating by optimizing electric field distribution.

Multichannel arrays of receiving coils are usually used to detect RF signals in clinical MRI systems. The standard number of receiver channels in an array is 16 or 32 (Fig. 2a), although it can be as large as 96 [65] in arrays designed for specific research purposes. An increase in the number of channels is motivated by the predominance of human body-generated noise in high and ultrahigh fields over noise in the receiving channel. It results in the phased array in the receiver regime ensuring a better signal-to-noise ratio than in volume coils (Fig. 2b–d), because each element of the receiver coil detects a noise signal coming only from the region immediately adjacent to a given coil element. To obtain a maximum signal-to-noise ratio, like in the case of transmitting arrays, individual receiver channels should be decoupled. For receiver channels this is a much simpler procedure, because their cross-coupling can be reduced by using special mismatched pre-amplifiers [43]. To avoid distortions in the signal B_1^+ field and disturbance of amplifier electronics, the receiving channels of a transceiver antenna system or a receiving coil operating independently of the transmitting one are switched off during transmission by a PIN diode system.

4. Metamaterials and dielectric structures for magnetic resonance imaging

One of the relatively new fields in ultrahigh field MRI technologies is the use of metamaterials, dielectric pads, and resonators. Metamaterials are artificial structures usually manufactured as a spatial combination of conductors and dielectrics. One of the characteristic features of metamaterials is that their components and the distances between them are significantly smaller than the wavelength of electromagnetic waves interacting with them. This property allows controlling

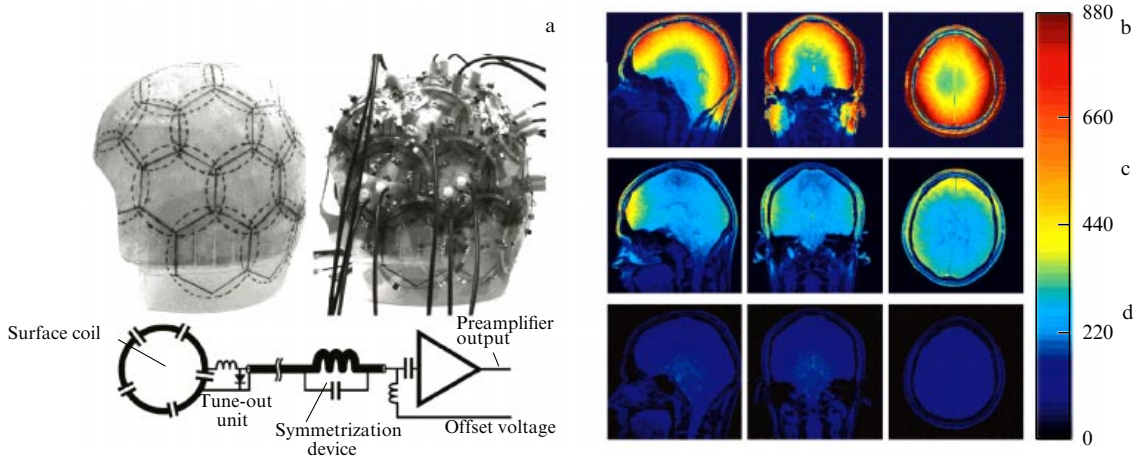

Figure 2. (Color online.) (a) 32-channel coil for human brain studies in a 3-T field and electric circuit of one receiver element. Signal-to-noise ratio distribution in human head for different receiver coils: (b) 32-channel coil, (c) commercial 8-channel coil, (d) commercial volume coil for head examination.

the effective permittivity (ε) and permeability (μ) of the medium, and even managing the negative values of these parameters. Although such effects are possible only in a relatively narrow frequency range, the metamaterial approach is still suitable for MRI, where the RF signals have a fractional frequency bandwidth close to 1%. The more important that material parameters management (at the Larmor frequency) can be done without using any sort of magnetic components. A metamaterial with a high or even negative μ value can be made of nonmagnetic parts, such as copper and plastic. This minimizes any unwanted interaction with a static magnetic field B_0.

Metamaterial-based devices can also be combined with standard MRI coils for redistribution of RF near-field components of the antenna element in a more efficient way (in terms of the signal-to-noise ratio value in the region of interest) as it already was demonstrated for 1.5 T MRI systems. The available free space inside of the typical scanner is limited due to the construction reasons. This began a trend of engineering metamaterial-based devices more compact by replacing bulk material slabs with metasurfaces.

The term metasurface from a theoretical point of view means just a two-dimensional metamaterial. After some simplification procedures, it can be created as a thin layer that still retains its original properties. Metasurfaces represented by planar arrays of parallel wires were tested in both high-field and ultrahigh-field MRI. Such an array can be considered as an anisotropic medium layer with high effective permittivity value but only for the electromagnetic waves polarized parallel to the wires and propagating within their plane. Near-fields of the array are spatially redistributed in a way providing maximum value of the magnetic field in the center while concentrating the electric field at the edges of the wires. In terms of MRI, this means improving the signal-to-noise ratio in objects located in the center of the structure. For exploiting this feature, the length of the wires must be tuned to half-wavelength resonant conditions. A more compact version of the metasurface can be made by combining conducting parts with dielectric insertions. After this modification, it can be placed right inside a standard head coil and improve the quality of the images by enhancing the RF magnetic field in the region of interest (Fig. 3). Designed as a soft pad, it does not cause any discomfort to the patient. Some more advantages like dynamic control of metasurface properties can be achieved using nonlinear and reconfigurable metamaterials.

The brain images (Fig. 3c, d) demonstrate a nonuniform signal intensity distribution over the scanned region caused by the RF-field interference and visible as bright and dark areas in the image. The wire metasurface does not eliminate this effect, as it is a result of field reflections in the brain tissues. However, this nonuniformity can be reduced by adding dielectric pads into the scanning setup. In comparison with metamaterial-based devices, dielectric pads have a more simple structure and are made of a single material with relative permittivity value equal to or higher than that of the scanned object ($80 < \varepsilon_r < 1000$). The presence of the pad changes the standing wave pattern and displaces the nodes of the field. For example, a pad in the form of a water bolus ($\varepsilon_r \approx 80$ placed near the patient's head eliminates the

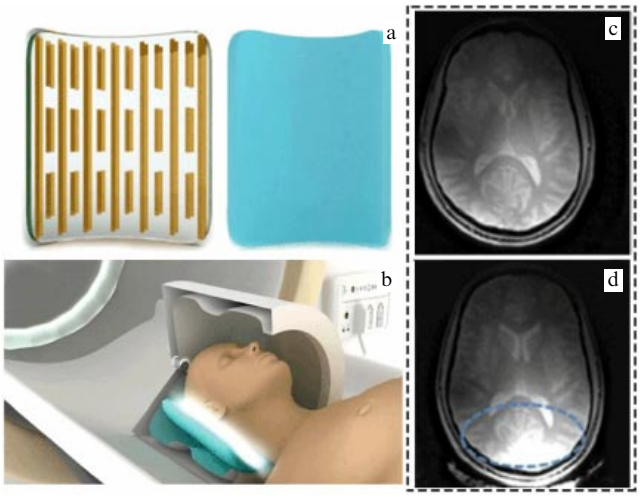

Figure 3. (Color online.) Flexible metasurface for RF field redistribution in ultrahigh (7 T) field MRI. (a) Structure of the metasurface formed from a combination of copper wires alternating with dielectric insertions. (b) Position of the device inside a conventional head coil. (c) Human brain image obtained without metasurface. (d) The same area scanned with the presence of the metasurface. The dashed line depicts the region of field enhancement.

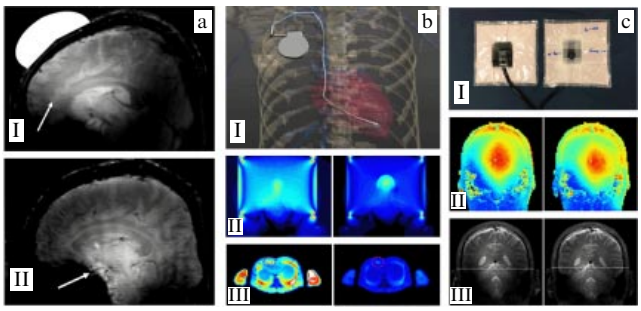

Figure 4. (Color online.) Nonresonant pads for field homogeneity improving in ultrahigh field MRI. (a) RF shimmimg with a water bolus in a 7-T field: I — signal intensity distribution in the human brain with the presence of the water bolus (arrow indicates maximum intensity region); II — signal intensity distribution in the absence of the water bolus and the corresponding position of the maximum intensity region. (b) Field distribution in a simulation with a human model equipped with a pacemaker in a 3-T field: I — patient model; II — field distribution in the head region in the absence (left) and presence (right) of a dielectric helmet; III — field distribution in the pacemaker region in the absence (left) and presence (right) of a dielectric helmet; the pacemaker position is depicted by the dashed line. (c) I — headphones combined with dielectric pads for a 7 T field applications: II — field distribution in the head region of a model in the absence (left) and presence (right) of the headphones; III — signal intensity distribution in experiment without (left) and with (right) headphones.

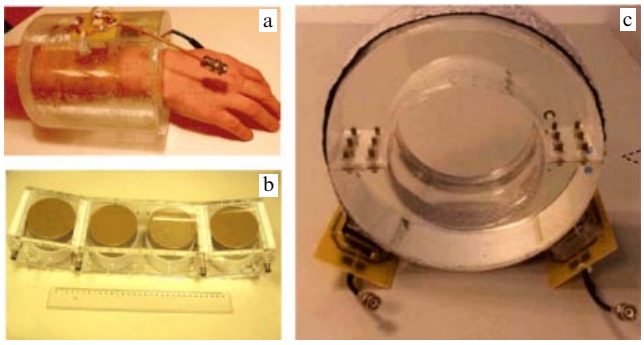

Figure 5. (Color online.) Dielectric resonant devices for ultrahigh (7 T) field MRI. (a) Resonator for wrist imaging. (b) Array of ceramic resonators for ultrahigh field MRI of the heart. (c) Resonator for knee joint scanning with a removable upper part.

destructive interference from the area of the brain and improves the uniformity of the RF field in the region of interest (Fig. 4a). It should be noted that such a procedure of increasing field homogeneity in the specified area or volume is referred to as RF shimming. Since dielectric pads do not need any additional energy sources, they provide so-called passive shimming.

The most common materials for the passive RF shimming are water and different kinds of ceramics like barium titanate ($BaTiO_3$) and calcium titanate ($CaTiO_3$). For ceramics, the relative permittivity value is in the order of several hundred or even thousands, that is why it is often used as a dielectric in the capacitors. A dielectric pad made of ceramics with $\varepsilon_r < 100$ improves the RF field homogeneity near its surface, which allows decreasing the amplitude of the exciting RF pulse without noticeable influence on the resulting image quality. This may be useful for the examination of the patients with pacemakers, for whom usual MRI procedures with a whole-body excitation can lead to possible harmful effects. Electromagnetic simulations of the brain scanning procedure with the human model equipped with a pacemaker demonstrate the local hot spots forming near the parts of the device, which are potentially dangerous for the patient. Ceramic pad shaped as a helmet preserves the high intensity of the RF field in the brain region, significantly decreasing the field that causes heating near the pacemaker (Fig. 4b).

During the MRI procedure, patients have to wear personal hearing protection equipment (headphones) to avoid a loud noise produced by the gradient coils. The same headphones are used for communication between the patient and technologist, so they are mandatory components of any modern MRI system. Headphones can be upgraded by adding a ceramic powder to its elements, which gives one more function of passive field shimming in a head region. This is the case, when dielectric pads can be used to improve the parameters of the clinical equipment without any intervention in its hardware (Fig. 4c).

All the dielectric pads demonstrated in Fig. 4 are nonresonant structures. However, a high value of permittivity also allows constructing volumetric structures resonant at the Larmor frequency. Such resonators can form eigenmode field patterns providing deeper control of the field distribution in space than simple nonresonant pads. The proper choice of the eigenmode can dramatically improve the excitation field pattern inside the object under investigation. The underlying idea is spatial separation of the electric and magnetic field components improving the signal-to-noise ratio. In this case, dielectric resonators are very close in their functional principle to the metamaterials mentioned above. One of the simple resonance structures is a hollow cylinder with the object placed inside of it. This type of resonator has different eigenmodes whose frequencies depend on the geometrical properties of the cylinder. One of them is the so-called transverse electromagnetic mode (TE-mode). At its frequency, the electric field is almost concentrated inside the dielectric and the magnetic field has its maximum inside the hollow, where it is polarized along the cylinder axis. Another eigenmode is the HEM-mode[2] characterized by the magnetic field component polarized orthogonal to the cylinder axis. The frequencies of both eigenmodes are close to each other, so it is possible to excite them together to achieve a circular polarization of the magnetic field inside the resonator. The biological object placed in the cylinder only slightly affects the field distribution of the eigenmodes, especially if the objects fit the dimension of the hollow [94].

This principle underlies the wrist coil for ultrahigh field implementation (Fig. 5a). A coil consists of a plexiglas cylinder filled by the distilled water and with an inner hollow diameter corresponding to the size of the hand. This design is relatively cheap and simple in comparison with conventional coils for the same purpose. The dielectric resonator is excited by two 50 mm loops. Despite the small size, they efficiently guide the energy at 298–299 MHz to the structure due to strong coupling with corresponding eigenmodes fields. The quality of the image provided by the coil can be comparable with multichannel coils for wrist imaging [94].

Ceramic resonators are characterized by higher relative permittivity than water; therefore, they have the smaller size needed for the formation of resonant structures. Due to this, they can be used to construct a phase array (Fig. 5b) where they play the role of antenna elements [95]. This design

[2] HEM-mode — hybrid electromagnetic mode.

combines the advantages of using a dielectric resonator and the standard approach for the formation of a multichannel array of receiver antennas. For example, this technology allows obtaining images of the thorax region with reduced field interference effects in the ultrahigh field.

In a previous case of dielectric cylinder coil [94], the construction represented a solid assembly. However, a coil design consisting of several parts that can be disconnected if necessary is more preferable for clinical routine. The plug-type connection inside the coil or on its surface facilitates the correct positioning of the object and assures relative comfort for the patient during examination. As a rule, a connection between the parts of the resonator corrupts the eigenmodes field distribution. Nevertheless, it is possible to restore the necessary modes by introducing conductors into the resonator structure. Thus, a detachable contact was created (Fig. 5c), in which conductors compensate field nonuniformity that develops in the region of the connection inside the dielectric and thereby contribute to the recovery of the resonator mode needed to examine a knee joint [96].

Combining traditional MRI technologies with the use of new materials and resonant structures opens up new prospects for improving the sensitivity of clinical systems, decreasing the duration of scan investigations, and reducing RF exposure in patients.

5. Waveguide magnetic resonance imaging

It was shown in Section 3 that a typical RF coil for MRI signal excitation in modern clinical high-field scanners with static magnetic field induction from 1.5 to 3 T is a birdcage resonator [29], first proposed in 1985. Both the design and the excitation method for such coil modes are described in Section 3. It is worth noting that the circular polarization of the RF magnetic field generated by such a coil doubles the energy efficiency of MRI (power consumption is reduced by half for the same field amplitude) compared to the energy efficiency of a so-called saddle coil that produces linearly polarized B_1 field (used in earlier MRI). The advantages of the birdcage coil are particularly pronounced in scanners with static magnetic field induction lower than 3 T. However, when such coils are used even in 3-T MR scanners, the homogeneity of the NMR signal excited in the human body decreases significantly, and the power consumption is twice as high as in coils in 1.5-T scanners. Such deterioration is due to the two-fold decrease in the RF signal wavelength and increased RF losses in the human body in the 130 MHz region, i.e., at the 3-T MR scanner operating frequencies [97].

Modern pre-clinical ultrahigh-field MR scanners with main magnetic field of 7 T cannot scan the whole human body at once. Although such systems are usually equipped with large-diameter (about 0.64 m) gradient coils capable of encoding an NMR signal in a region comparable to the size of the human body, a versatile coil that could excite an NMR signal over such a large spatial area does not exist yet. The design of birdcage coils can not be adapted for 7-T field tomographs.

It was mentioned above that the operation principle of such a coil is based on resonance conditions of the RF current flow among its two rings and longitudinal rods; therefore, if the resonant frequency is doubled at a fixed diameter, the resonant rod length will decrease significantly [97]. As a result, the birdcage coil becomes unsuitable for NMR signal excitation in the whole human body in a scanner with a 7-T or higher field strength. Today, MR images are acquired in ultrahigh field scanners with local excitation coils designed for particular body parts. Such coils are directly placed on the body surface of the patient to provide necessary RF magnetic field magnitude within a limited region. The absence of an efficient versatile coil for large-area scanning in 7-T MR scanners is the main obstacle for clinical application of ultrahigh field MRI scanners.

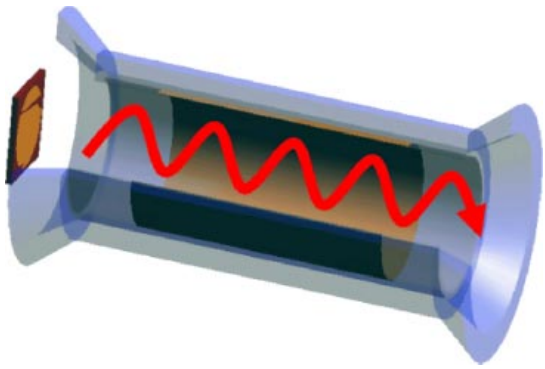

Figure 6. Use of a scanner bore as a waveguide for human diagnostics. The RF signal propagates along the bore axis that plays the role of a cylindrical metallic waveguide at a frequency of around 300 MHz (7-T field MRI operating frequency). The signal is transmitted and received by a coil at the left end of the bore. There is almost complete reflection of signal from the right end because the radiation from the open end of the single-mode waveguide is insignificant.

The relatively small wavelength of an RF signal in ultrahigh field MR scanners is not always a disadvantage. For example, at 300 MHz the metal bore of the scanner turns into a part of a cylindrical waveguide (Fig. 6) that transfers the flux of the RF electromagnetic field from the antenna at one end of the bore to its other end. Indeed, according to the well-known formula for the cut-off frequency of the first fundamental (TE_{11}) mode of a circular hollow metallic waveguide with diameter d filled with a medium having absolute permittivity ε and absolute permeability μ,

$$f_c = \frac{1.841}{\pi d\sqrt{\mu\varepsilon}} .$$

For a standard bore diameter of 0.6 m, we have $f_c = 293$ mHz. In fact, this frequency is somewhat lower because the human body fills the bore partly. Frequencies near 300 MHz corresponding to MRI with a 7-T field are lower than the excitation frequencies of the next (TM_{01}) mode that is equal to 381 MHz for an empty bore. Therefore, it is the 300 MHz region where losses in metal turn out to be minimal during the propagation of radiation along the bore.

Ultrahigh field MRI with waveguide-based RF signal transmission is also known as traveling-wave or waveguide MRI [98]. The possibility of using a waveguide as an energy-efficient system for excitation and detection of high-field NMR was noted as long ago as 1977 [99]. However, the size of the proposed waveguides proved incompatible with bore diameters used at that time. Therefore, special transmission lines were developed to implement this principle [99].

Waveguide MRI has several potential advantages over MRI using conventional RF coils and even coil arrays with parallel RF signal transmission. First, the waveguide technology allows obtaining MR images of large regions limited only by the size of the scanner bore and gradient coils. Second, the remote location of the transmitting coil assures comfort and

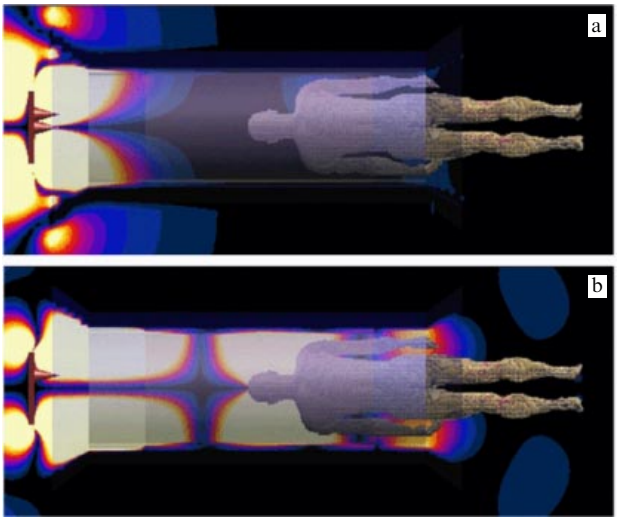

Figure 7. (Color online.) Use of waveguide MRI for human body diagnostics is possible only if a static magnetic field induction is 7 T or higher, because in such a case the RF signal wavelength is comparable to the scanner bore diameter. (a) 1.5-T scanner field distribution. The bore is too short compared to the scanner operating wavelength (~ 4.7 m), thus, the RF signal does not propagate along the bore. (b) In a 7-T scanner, the RF signal propagates along the bore axis, and a standing wave forms due to the reflection from the ends of the bore.

safety for the patient. In addition, such coil position allows space for additional equipment, e.g., stimulation systems for functional MRI.

The waveguide technology can be implemented only in ultrahigh field MRI with the formation of a standing wave (Fig. 7b) due to internal reflection of the wave from the bore ends. The propagation of such a wave is impossible in the standard-sized scanner bore at operating frequencies of devices with magnetic field induction lower than 7 T (Fig. 7a). The presence of a standing wave should be taken into consideration for the patient position in the bore [100–103]. However, the standing wave can be avoided by matching the bore ends to free space via attaching electrodynamic loads along the perimeter of the bore's end. However, this solution will lead to the RF signal energy losses: absorption loss or loss via radiation from the bore ends. It is also possible to tune the position of the standing wave node. For this aim, electrodynamic loads should be placed inside the bore. Axially oriented straight wires arranged at a distance from the bore wall can be employed as such loads (such a loaded waveguide is called a coaxial waveguide [103]). It should be mentioned that in a loaded waveguide, one or two highest-order modes can be excited, and their interference with the fundamental mode can be used for shimming [102, 103].

Currently, waveguide MRI is a separate field of research, and its purpose is the development of a versatile coil suitable for scanning the whole human body in ultrahigh magnetic fields. The main potential advantages of the waveguide-based method have already been demonstrated by the present moment: it allows visualizing large volumes [100, 101] and provides an opportunity to control RF magnetic fields in the human body [102, 103]; an important fact is that this method is compatible with local receive coils arrays [104, 105]. However, the ratio of the transverse RF magnetic field magnitude to the power consumption of the antennas that are used in waveguide MRI remains too low, especially compared to the local excitation elements. In addition, the peak power values of the RF amplifiers in ultrahigh-field preclinical MR scanners are significantly limited compared to the clinical MR scanners. As a result, clinical MR sequences, most of which require large amplitude of transverse RF magnetic fields, are currently incompatible with waveguide MRI, thus, its application in MR scanning of the human body in ultrahigh magnetic fields is seriously limited.

6. Functional magnetic resonance imaging

The notion of functional MRI integrates a variety of studies yielding a series of MR images of any healthy or diseased organ performing its function. However, the term most frequently implies MR studies of the human brain.

The most popular fMRI method is the one based on blood oxygen level dependent (BOLD) contrast. It produces a series of brain images taken during the performance of preformulated tasks or at rest. BOLD fMRI makes possible the detection of disturbances in the blood supply to brain tissues during the transition from resting to active states by recording an accompanying NMR signal intensity jump caused by the difference in relaxation parameters of the tissues as blood moves in them at rest or in the active state.

In the scope of the transition from fMRI studies with high field scanners to those based on the use of ultrahigh field machines, the sensitivity of the BOLD method is affected by changes in the NMR signal amplitude in the ultrahigh field and alteration of brain tissue relaxation parameters, gradually leading to a change in the fMRI procedure and its purpose.

The signal-to-noise ratio in MR scanning is considered to be proportional to magnetic field induction or even the square root of it (when accounting for the increase in the receiver tract frequency band at the higher operating frequency of the MR scanner) and to the cube of the spatial resolution [106, 107]. In this approximation, transition from the standard fMRI 3-T field to the 7-T field allows a 1.15- or 1.33-fold increase in isotropic spatial resolution.

On the other hand, the rapid development of new RF devices to be operated in ultrahigh fields poses the problem of an ideal signal-to-noise ratio attainable for a given scan object or a class of such objects, in particular, for various degrees of accuracy of the human head model. Numerical calculations have shown and subsequent measurements confirm (Fig. 8) that the creation of a certain configuration of currents around the subject of interest allows a nonlinear (with an exponent greater than unity) increase in the signal-to-noise ratio upon a change in magnetic field induction [108–110]. Experimental studies on the dependence of the signal-to-noise ratio on the static field induction strength also demonstrated the nonlinear growth of this ratio: at the center of the human head in a 7-T field it is 3.36 times that in a 3-T field. In contrast, the difference is less pronounced in outer cortical layers, where the signal-to-noise ratio increases only by a factor of 2.96 [111]. Thus, the transition to an ultrahigh field produces an approximately 1.5-fold improvement in the resolving power. As a result, the spatial resolution of fMRI images approaches the borderline value between macro- and mesoscopic methods. Thus, high-field fMRI (1–3 T) detects activation of brain regions 3–5 mm^3 in volume [112, 113], while the transition to an ultrahigh field permits reducing the voxel[3] size to

[3] A voxel is an element of a 3D image (the analog of a 2D pixel for three-dimensional space).

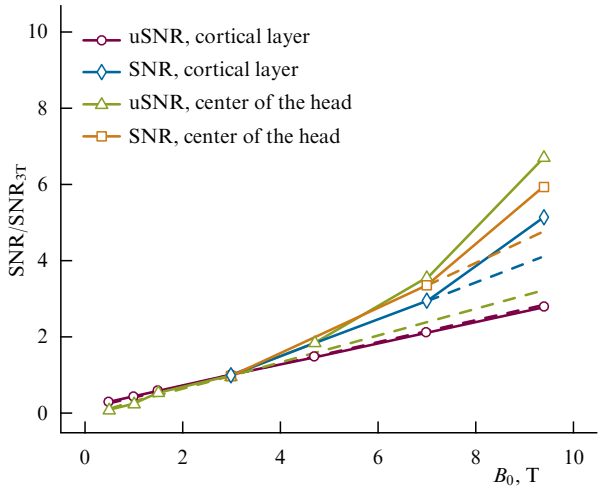

Figure 8. (Color online.) Experimentally obtained signal-to-noise ratios (SNRs) and results of numerical simulation of the signal-to-noise ratio in the case of ideal current distribution around the scanned object (uSNR) measured in the brain cortical layer and in the center of the head. Dashed lines indicate linear approximations of signal-to-noise ratio dependences in each case. Each dependence is normalized to the signal-to-noise ratio in field $B_0 = 3$ T. Evidently, the signal-to-noise ratio grows with increasing magnetic field induction faster than for the linear approximation in all cases except uSNR modeling in the cortical layer.

submillimeter values [114, 115] and thereby displaying the activation of individual cortical columns.

An even more important source of focusing the BOLD-fMRI method on submillimeter structures in ultrahigh fields is a relative change in relaxation parameters of intra- and extravascular blood tissues and brain structures related to vessels of various diameters. Systematization of data on blood relaxation properties makes it possible to formulate empirical dependences of the magnitude of MRI signal changes in BOLD fMRI on vessel diameter, blood saturation with oxygen, and magnetic field strength. Moreover, the BOLD response depends on the pulse sequence being used by virtue of different relaxation mechanisms detected in sequences based on spin [116] and gradient [117] echoes.

Analysis of the dependences thus obtained indicates that in the case of gradient echo-based sequences there are no conditions (Fig. 9b) at which a signal coming from small vessels (up to 0.02 mm in diameter) dominates over a signal from large vessels (0.2 mm or more). At the same time, if spin echo-based sequences are used (Fig. 9a), the ratio of these two signals reaches a maximum value in fields of 4–8 T, whereas it does not exceed unity in fields of up to 3 T [118]. It can be concluded that the BOLD response registered in ultrahigh fields is associated with structures with a characteristic size of several dozen micrometers, whereas the response in high fields is largely associated with structures measuring tenths of a millimeter.

7. Diffusion-weighted magnetic resonance imaging

Sensitivity to random molecular motion (diffusion) in MRI gives rise to a number of diagnostic and research methods, such as Diffusion Weighted Imaging (DWI), Diffusion Tensor Imaging (DTI) [9], Diffusion Spectrum Imaging (DSI) [119], and their modifications [120, 121]. Methods providing information on principal directions of diffusion (DT, DSI, etc.) are based on the computation of several self-diffusion coefficient distribution maps (as in DWI) differing in the direction of diffusion measurement and the influence of diffusion on the registered signal intensity (diffusion weighting). Due to this, factors acting on diffusion-weighted images just as well affect data obtained using more sophisticated techniques.

As in the case with fMRI, the first factor influencing results of diffusion-weighted MR scanning is the growth of the signal-to-noise ratio with increasing magnetic field. It results in a significant improvement of spatial resolution of diffusion-weighted imaging when transitioning from high to ultrahigh field MRI. On the other hand, the signal-to-noise ratio in classical diffusion-weighted spin-echo sequences (Spin-Echo Echo-Planar Imaging (SE-EPI) depends on transverse relaxation time T_2. The main tissues of interest for DTI (first and foremost, the brain white matter and other myelinated neural pathways) exhibit a decrease in T_2 with increasing magnetic field. This results in the relative weakening of the echo signal observed at a fixed time T_{echo} of the echo signal registration, which, in turn, leads to a decrease in the signal-to-noise ratio. If relaxation phenomena and other effects influencing the signal-to-noise ratio are taken into consideration (e.g., an increase in the receiver channel

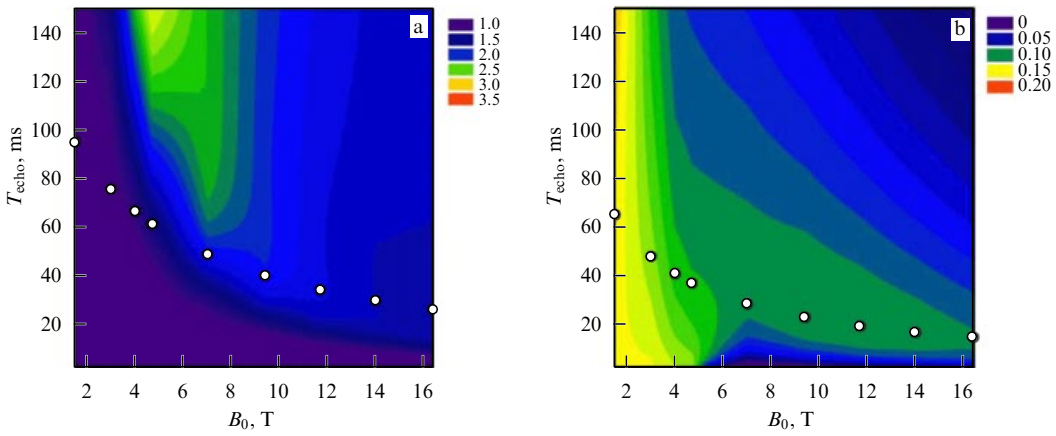

Figure 9. (Color online.) Dependence of the ratio of BOLD response associated with small vessels to the BOLD response associated with major vessels on static magnetic field induction B_0 and echo signal observation time T_{echo} for (a) spin echo- and (b) gradient echo-based sequences. Note the scale difference in Figs a and b.

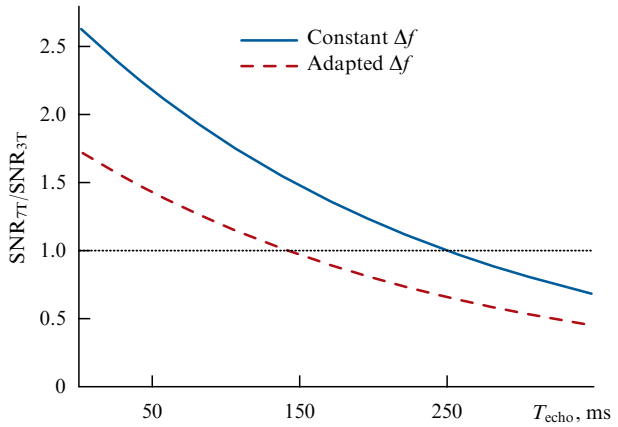

Figure 10. Simulated dependence of signal-to-noise ratio in a diffusion-weighted pulse sequence in 7-T (SNR_{7T}) and 3-T (SNR_{3T}) fields as a function of echo signal observation time T_{echo}. Simulations consider the cases of constant transmission band Δf of the receiver and of an adapted Δf where the band increase is required for mitigating image artifacts in higher fields. The dotted line indicates the level of equal signal-to-noise ratios in two simulations.

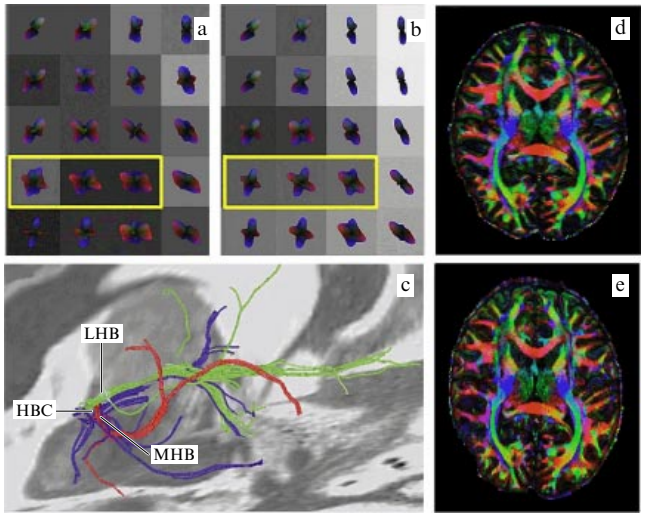

Figure 11. (Color online.) Results of diffusion-weighted imaging in ultrahigh fields. (a) The map of orientation density function (the angular component of particle displacement probability density) corresponding to the principal diffusion directions measured in a 3-T field. (b) Similar mapping measured in a 7-T field. More pronounced distributions in the ultrahigh field allow a more accurate assessment of diffusion anisotropy; this effect is most noticeable in the region enclosed in the yellow rectangle. (c) Reconstruction of nerve fibers coming out from the lateral habenular (LHB) and medial habenular (MHB) of the epithalamus and habenular commissure (HBC) based on the results of ultrahigh field (7-T) scanning. The difference between nerve fibers is revealed by virtue of submillimeter resolution of initial data. (d) Results of the reconstruction of nerve fiber direction in the entire brain (a single layer is shown) based on high field (3-T) scan data. Similar results obtained for the same patient in the ultrahigh (7-T) field demonstrates a more detailed image and more accurate assessment of diffusion anisotropy (represented as brighter image).

frequency band for the compensation of scanning artifacts in an ultrahigh field and reduction in the number of steps of so-called phase coding), the signal-to-noise ratio for a classical diffusion-weighted sequence in the ultrahigh field proves higher than, for example, in 3-T clinical fields, but only within a certain range of T_{echo} values (Fig. 10). This advantage of MRI with $B_0 = 7$ T over that of MRI with $B_0 = 3$ T is apparent at equal transmission bands of the receiving channel if T_{echo} is shorter than 250 ms. In the case of an adapted transmission band, the advantage of ultrahigh field MRI disappears when T_{echo} exceeds 150 ms [122].

The nontrivial constant magnetic field dependence of the signal-to-noise ratio is complicated in DWI by the difference in the values of the latter in images with different diffusion weighting acquired within the framework of a single experiment. Using such data to calculate anisotropic diffusion parameters (fractional/partial anisotropy, mean diffusivity, etc.) leads, in turn, to the dependence of the calculated values on the strength of the static magnetic field. Increasing the field is associated with a marked rise in fractional anisotropy and a decrease in mean diffusivity [123, 124]. Evidently, the influence of the magnetic field on diffusion itself in MRI is minor and the observed effect should be regarded as a result of specific features of the diffusion measurement process. Indeed, it was shown that scanning under thorough T_{echo} and signal-to-noise ratio control results in the measurements of anisotropic diffusion parameters in high and ultrahigh fields coinciding [125, 126]. Moreover, it was demonstrated in [127] that setting an experiment in an ultrahigh field (with equal scan parameters) yields more accurate anisotropy parameter distribution maps due to a higher signal-to-noise ratio (Fig. 11a, b).

An increased signal-to-noise ratio allows use of nonstandard sequences for diffusion-weighted scanning in ultrahigh fields, e.g., diffusion-weighted turbo spin-echo [128], less sensitive to artifacts related to field nonuniformity than in the traditional SE-EPI method. The enhanced signal-to-noise ratio makes possible targeted diffusion-weighted scanning of miniature regions, such as the habenula (part of the epithalamus) [129] and nerve fibers passing through them (Fig. 11c). In whole-brain imaging, the enhancement of the signal-to-noise ratio produces much more distinct anisotropic diffusion maps, despite a smaller amount of collected data [130] (Fig. 11d, e). The use of an ultrahigh field in pre-clinical studies ensures ultrahigh resolution (less than 0.05 mm in a 9.4-T field) when mapping the self-diffusion tensor [131, 132], estimating post-traumatic regeneration of peripheral nerve branches, detecting posttraumatic changes in the central nervous system [134–136], and observing myelination of cerebral pathways [137, 138].

8. Magnetization transfer in chemical exchange

When performing MRI in fluids, solute and solvent are observed in one of the two modes: rapid or slow exchange, depending on temperature, chemical composition, frequency of resonance, and other parameters. Each of the two regimes is characterized by a specific relationship between the chemical shift difference of the resonances of two NMR-active nuclei populations and the rate of nuclei exchange between them. In classical NMR spectroscopy, slow exchange corresponds to the observation of two spectral lines from each population, and rapid exchange to the observation of a single resonance line averaged over two populations.

In traditional tomography, an NMR signal is usually considered to be a single spectral line of free water; nevertheless, the observation of a solute/solvent system in the slow exchange regime can provide the spatial distribution of solute via narrow-band saturation of its resonance lines and detection of a decrease in the free water signal during

exchange (the chemical exchange saturation transfer method — CEST).

The efficiency of magnetization transfer (i.e., sensitivity of the method) is estimated in various ways. The simplest criterion is the proton transfer ratio (PTR), calculated as the ratio of the change in amplitude of a signal from a large nucleus population S_w to the amplitude of the initial signal from this population S_{0w}. If the exchange occurs between two populations with a large difference between equilibrium population densities (and equilibrium exchange constants), PTR can be related, as in [139], directly to the constants of relaxation R_{1w}, R_{1s}, and exchange k_{sw} of the two populations (corresponding to indices s and w):

$$\mathrm{PTR} = \frac{S_{0w} - S_w}{S_{0w}} = \frac{k_{sw}\alpha x_{CA}}{R_{1w} + k_{sw} x_{CA}} \left\{1 - \exp\left[-(R_{1w} + k_{sw} x_{CA}) t_{sat}\right]\right\},$$

where t_{sat} is the length of the pulse saturating resonance of the dissolved substance, x_{CA} is the ratio of the number of resonant nuclei involved in the exchange to their total content in the solvent, and α is a quantity depending on relaxation and exchange constants characterizing resonance saturation efficiency ($\alpha = 1$ if the peak is completely suppressed).

Exchange efficiency is also characterized by the degree of proton transfer enhancement (PTE), i.e., the PTR normalized to x_{CA}. However, neither the PTR nor PTE takes into account the broadband magnetization transfer and suppression of the solvent signal by the saturation pulse. To take into consideration these factors and the dependence on the saturation pulse carrier frequency, the magnetization transfer ratio (MTR) is introduced, which can be represented as the sum of components corresponding to different sources of change in the observed signal:

$$\mathrm{MTR}(\Delta\omega) = 1 - \frac{S_w(\Delta\omega)}{S_{0w}(\Delta\omega)} = \mathrm{PTR}(\Delta\omega) + \mathrm{MTC}(\Delta\omega) + \mathrm{DC}(\Delta\omega),$$

where magnetization transfer contrast (MTC) is the term responsible for broadband magnetization transfer, and direct contrast (DC) is the term responsible for direct saturation of solvent resonance by the saturation pulse. The dependence of the MTR on the difference between saturation and solvent resonance frequencies $\Delta\omega$ is also referred to as the z-spectrum or CEST-spectrum. A PTR value is obtained experimentally from the fact that both direct saturation and broadband magnetization transfer are symmetric with respect to the solvent resonance frequency, while the PTR depends only on the presence of the solvent resonance peak at the irradiation frequency; therefore, the following expression holds for most substances:

$$\mathrm{MTR}_{assym}(\Delta\omega) = \mathrm{MTR}(\Delta\omega) - \mathrm{MTR}(-\Delta\omega) = \frac{S_w(-\Delta\omega) - S_w(\Delta\omega)}{S_{0w}(\Delta\omega)} = \mathrm{PTR}(\Delta\omega),$$

due to the absence of solute peak at frequency $-\Delta\omega$.

Clearly, the efficiency of the CEST method directly depends on k_{sw}, because the more nuclei comprising the saturated magnetization are transferred from the solute to the solvent, the greater the change in the solvent signal.

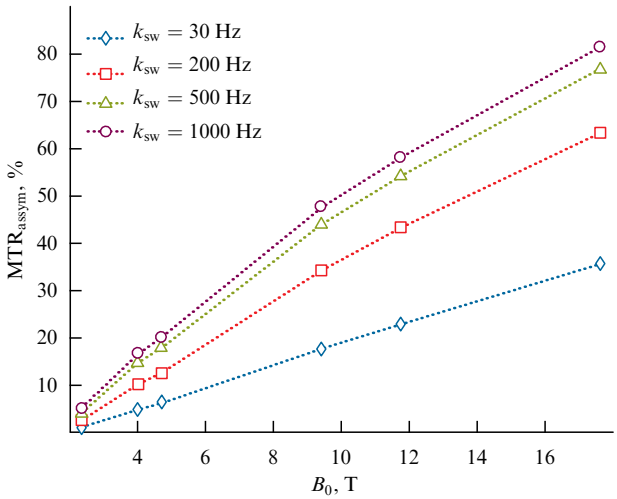

Figure 12. (Color online.) Calculated dependences of the observed CEST effect on the magnitude of the magnetic field for a single peak (with a chemical shift of 3.5 ppm) in the cortical tissues of a murine brain. Increasing the magnetic field allows the observation of faster exchange and enhances the efficiency of z-spectrum registration.

However, the necessity to observe the z-spectrum in the slow exchange regime (i.e., at $\Delta\omega \gg k_{sw}$) requires transition to a stronger magnetic field for observation of exchange with high k_{sw}, because $\Delta\omega \sim B_0$ for two arbitrary substances. A rise in k_{sw} is associated with a decrease in the saturation efficiency parameter α, since more nuclei from the unsaturated solvent population enter the solute population. In this case, α can only be improved via increasing the saturation pulse power, which is rarely possible *in vivo* due to restrictions on RF power deposition in living tissues. On the other hand, increasing the static magnetic field is associated with a change in relaxation characteristics R_{1w} and R_{1s}, which, in turn, results in a significant increase in the observed CEST effect [140]. The total effect of increasing the static magnetic field can be calculated (Fig. 12) by considering the values of relaxation parameters in different fields [139].

The improvement in CEST MRI efficiency in an ultrahigh field allows developing potent hydroxo and amino group-based CEST agents for the detection and identification of cancerous neoplasms [141–143], the analysis of central nervous system activity [144], and injuries to the cartilage tissue [145] often inapplicable in lower magnetic fields due to small chemical shift [146]. CEST MRI based on proton exchange with hydroxo and amino groups also finds wide application for tumor diagnostics and in pre-clinical ultrahigh field MRI [147, 148]. In addition, magnetization transfer technologies are successfully employed in pre-clinical MRI for noninvasive measurement of tissue acidity [149–152], ischemic stroke detection based on minor chemical changes [153], and other applications [154–158].

9. Image reconstruction from an incomplete data set

Reconstructing an initial function from an incomplete data set is a classical signal processing problem [159]. In this context, data incompleteness is understood as a deviation from the Nyquist criterion, i.e., as data sampling at a mean frequency of less than twice the signal maximum frequency. The mean frequency is defined as the total number of

recorded counts divided by the total duration of data collection. However, a direct reduction of the sampling frequency (keeping the sampling uniformity) is fraught with errors in image reconstruction and artifacts hampering clinical interpretation of the images [160]. For this reason, correct reconstruction requires incoherent sampling and nonlinear procedures comprising together the compressed sensing algorithms. These algorithms are also referred to as l_1-optimization, because from the mathematical standpoint, they serve to minimize the l_1-norm of image sparse representation, i.e., to find x that minimizes the functional:

$$\min \|\Psi x\|_1 ,$$

on condition that

$$\left\|\mathrm{FT}(x) - y\right\|_2 < \varepsilon ,$$

where x is the reconstructed image being sought, Ψ is the transformation converting x into a sparse form, FT is the Fourier transform (or other transform if appropriate for image reconstruction), y is the sampled signal, and ε is a parameter characterizing image reconstruction accuracy [160].

Compressive sensing finds application due to information redundancy contained in the phase space. Skipping the corresponding parts at the acquisition stage decreases the number of sampling steps and significantly reduces the MRI scan duration without substantial loss of image quality. The use of this algorithm in high field (up to 3 T) MRI allows performing studies requiring high resolution and signal-to-noise ratio along with the shortest data collection period, e.g., certain dynamic contrast enhancement modalities [161–163], angiography [164–166], and other applications [167–169]. The requirement of high signal-to-noise ratio and resolving power is usually met in ultrahigh field MRI (over 3 T) by virtue of improved signal amplitude and strong gradient pulses, however, the improved spatial resolution is accompanied with a longer data collection time which significantly impairs temporal resolution of the study.

It can be concluded that the efficiency of a transition to an ultrahigh field decreases without the use of methods for enhancing temporal resolution frequently based on compressed sensing algorithms. In particular, clinically-oriented applications have demonstrated a high efficiency of compressed sensing-based reconstruction in high-resolution angiography [170–173], ultrafast fMRI [174], and heteronuclear MRI [175, 176] studies. Compressed sensing in preclinical applications was successfully employed to create new distortion-resistant pulse sequences for fMRI [177], visualization of fluid flows at the microscopic level [178], ultrafast registration of dynamic contrast amplification [179], significant acceleration of relaxation time measurement in biological subjects [180], and the generation of high-resolution heteronuclear images [181].

For ultrahigh resolution time-of-flight angiography of human brain vessels (with a voxel size of $0.28 \times 0.28 \times 0.28$ mm^3), incoherent data collection and reconstruction making use of the difference between the neighboring elements as Ψ allows an almost four-fold reduction of time (Fig. 13a). The use of the compressed sensing algorithm to obtain sodium distribution maps in human joints (omitting from half to three quarters of the collected data without sparse transformation, i.e., at $\Psi = 1$) resulted in the successful reconstruction of images with a two-fold reduction in data collection time. However, higher compression was associated with deviation from the calculated sodium levels in certain parts of the images (Fig. 13b). Visualization of a fluid velocity map on a chip (Fig. 13c) allowed reducing the scan duration by 16 times, while preserving the reliable map of fluid velocities in microvessels. In this case, wavelet basis expansion (particularly, symmlet basis expansion) was used as sparse transformation Ψ.

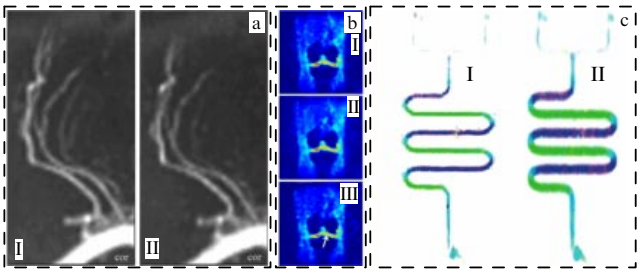

Figure 13. (Color online.) Results of application of compressed sensing algorithms in an ultrahigh field (7 T). (a). Ultrahigh resolution time-of-flight angiography in the field: I — image acquired by the conventional data collection method (data collection time ≈ 9.5 min), II — image acquired using compressed sensing algorithms (data collection time ≈ 2.5 min). (b) Maps of sodium distribution in the knee joint obtained: I — by the classical radial data collection method (data collection time ≈ 17 min), II — with a two-fold incoherent reduction in the amount of collected data, III — with a three-fold incoherent reduction of the amount of collected data (arrow shows the region where concentration deviates from the control value). (c) Map of velocities in microchannels obtained: I — using a compressed sensing algorithm (resolution 256×256 pixels), II — by the classical method for the same time (resolution 63×63 pixels).

Thus, the use of the compressed sensing makes it possible, depending on the object of study and data collection algorithm, either to reduce the study duration by almost 16 times without detriment to the image quality or to carry out an experiment with improved resolution in the same time.

10. Magnetic resonance fingerprinting

The transition from the classical data collection strategy to more efficient modern methods is not limited to pseudorandom filling of the k-space (see Section 9). The MR scanning process itself can undergo substantial modification.

At present, the majority of MRI data is collected in the framework of MR scan protocols consisting of MR sequences, each giving (according to its type and parameters) one or more image series with a specific relationship between NMR signal intensities from different tissues, so-called image weighting. The signal intensity in such weighted images is determined first and foremost by the relaxation characteristics of the respective tissues, however, the relaxation parameters themselves are not measured. Nevertheless, such parameters can be measured, yet in this case relatively long sequences are used, allowing taking into account the influence of a selected parameter on NMR signal intensity and disregarding the influence of the others. The resulting dataset is then further processed to calculate such parameters as longitudinal and transverse relaxation times or self-diffusion coefficient [182–186]. On the other hand, the necessity to separate the influence of parameters not measured in a particular experiment means that, for an arbitrary choice of scan parameters, the contribution to MRI signal intensity comes from many characteristic para-

meters of the tissue. This fact changes the paradigm of numerical assessment of relaxation (relaxation times T_1, T_2, or T_2^*) and other (e.g., self-diffusion coefficient, magnetic susceptibility) characteristics of the tissues in MRI and gives rise to the appearance of a method of MR fignerprinting of biological tissues [187].

This method is based on the dependence of an NMR signal recorded in an arbitrary pulse sequence on the complete set of relaxation and other characteristics of the imaged tissue. Because the MRI signal depends on the totality of tissue properties, its value for a given pulse sequence at a certain moment can be unique for a tissue characterized by a specific set of properties. Clearly, for a particular relationship between tissue and sequence parameters, the signal can be identical for two types of tissues having different properties. Therefore, in order to be able to accurately relate the signal parameters to tissue characteristics, one uses, first, a sequence with a random set of pulses and, second, a large number of consecutive NMR signals. Such a set is unique for each set of tissue parameters measurable by NMR (i.e., for a particular tissue), even if signal values from two tissues at a single point in time coincide. Therefore, it can serve for tissue identification exactly as fingerprints do for personal identification (hence, the name of the method: magnetic resonance fingerprinting).

An important aspect of magnetic resonance fingerprinting is the process of identifying a series of signals. It includes the use of arrays of simulated series of signals (dictionaries) in which each series corresponds to a certain set of measurable tissue characteristics. Coincidence of measured and dictionary signals makes tissue identification possible and thus provides its relaxation and other parameters. Evidently, the number and spread of the parameters, as well as dictionary resolution in parametric space, determine both the coincidence search rate and the amount of computer memory needed to work with the dictionary. To reduce the search time and requirements, various compressed sensing and coincidence detection algorithms are used [187–193].

The usual variables included in the dictionary are relaxation times, relative spin density, and static field B_0 value (or degree of its nonuniformity for the characteristic of the magnetization's nonresonant behavior). In high-field scanning, such a set of parameters allows relaxation times to be efficiently determined in healthy and pathological cerebral tissues [194] and normal eye [195], abdominal cavity [196], and myocardium [197] tissues. Inclusion of the self-diffusion coefficient in the scan protocol allows prostate cancer stages to be detected and determined [198]. The use of the fingerprinting method in pre-clinical MRI makes it possible to reduce the influence of physiological movements (much more pronounced in small laboratory animals than in humans) on measured relaxation time [199].

RF field inhomogeneity manifesting itself upon a transition to clinical scanning in ultrahigh fields has a detrimental effect on the accuracy of tissue recognition by the MR fingerprinting method. This aggravated inhomogeneity problem requires finding a fundamental solution when going to 7-T and higher fields. In the context of MR fignerprinting, such an approach comprises introducing additional dimensions entering into the fingerprint dictionary of simulated signals, corresponding to parameters responsible for possible RF field variations in the RF coils used during the MR scan.

Direct realization of RF field nonuniformity correction employs introducing the flip angle as one of the parameters of the fingerprint dictionary (and, accordingly, as an additional dictionary dimension) [196]. Measurements of phantom relaxation times with and without such correction showed that measured T_2 times are most sensitive to RF field inhomogeneities, whereas the accuracy of T_1 time recognition remains practically unaltered in the absence of corrections to alternating field inhomogeneities (Fig. 14). An even higher measurement accuracy is achieved if elements increasing signal sensitivity to the RF field variations are included in the sequence used to generate an MR fingerprint. An example of such element is a series of pulses with a sharp change in the flip angle that disturb the course of a classical steady-state sequence for recording an MR fingerprint [200].

However, whatever method is used, the problem of RF field inhomogeneity correction via its inclusion as a parameter in the recognition dictionary consists in the inability of correcting high deviations of the RF field from the nominal value. A significant deviation of a real alternating magnetic field from the desired one accounts for the appearance of regions in which RF pulses of the MR fingerprinting sequence does not provide a large enough flip angle (over 5°) from equilibrium position. In such a case, MR fingerprints of

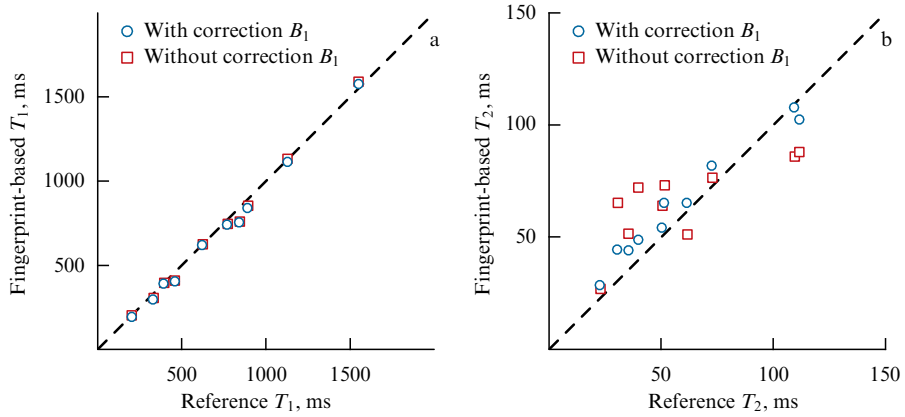

Figure 14. (Color online.) Results of the measurement of relaxation time by the magnetic resonance fingerprinting technique in a 3-T field. Measurement of (a) T_1 time and (b) T_2 time. Real relaxation time is determined by classical NMR methods. Accuracy of the measurement using magnetic resonance fingerprinting depends on the proximity of the point to the diagonal (dotted line). Evidently, correction of RF field inhomogeneities does not affect the accuracy of measurements of longitudinal relaxation but ensures better agreement with results obtained by classical methods for the measurement of transverse relaxation.

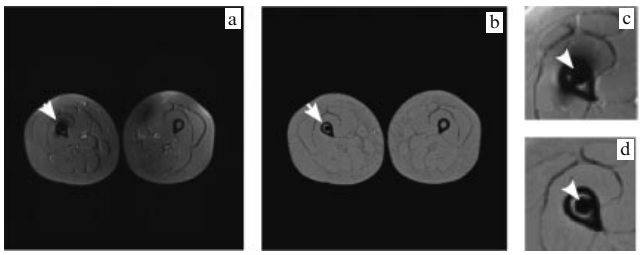

Figure 15. MR images of human extremities with a surgical implant acquired with the use of (a, c) classical invertion-recovery sequence with data collection by turbo spin-echo imaging and (b, d) MR fingerprint method with variable excitation by different transmitting coil modes. Figures (a) and (b) show that implant-related artifacts manifest themselves not only in the region of the metal rod location (indicated by the arrow) but also in the contralateral extremity. Magnified images of implant location region in Figs c and d suggest that the MR fingerprint method allows obtaining an image in the 3-T field without artifacts, even in immediate proximity to the implant.

substances differing in relaxation times become indistinguishable. This ambiguity can be eliminated by using the RF magnetic field distribution properties of different modes of the birdcage coil employed to generate the RF magnetic field in the majority of scanners. For example, field minima (representing problematic recognition areas) of coil degenerate circular polarization modes CP_1 and CP_2 [201] are spaced far apart. Due to this, excitation of different coil modes within a single sequence results in the generation of a unique imprint, regardless of the presence of the field minimum at the object location point, because the single mode minimum position at this point is compensated by the maximum of another mode located at the same point. Further inclusion of measured field distributions over two coil modes in the MR fingerprint dictionary allows avoiding errors of recognition associated with strong RF field nonuniformity [202]. Moreover, the method in question allows MR studies in anatomical regions where RF field nonuniformity is due to the presence of metal objects (e.g., surgical implants) rather than to the properties of the exciting coil modes (Fig. 15).

11. Heteronuclear magnetic resonance imaging

Magnetic resonance spectroscopy (MRS) is a nonionizing technique used to determine the chemical composition and observe metabolic processes in living tissues under natural conditions. In vivo application of MRS provides a powerful tool for the noninvasive detection of cellular metabolites, measurement of the metabolic rate, energy exchange, and neurotransmission in the brain and other organs, as well as for the study of changes in these processes caused by physiopathological disorders.

MRS of hydrogen nuclei is the most common clinical implementation of this technique, since any MR scanner is commonly equipped with all instrumentation necessary for its realization. However, a few more nuclei producing an MR response, besides hydrogen, occur in living organisms (see the table). Heteronuclear MRS is designed to detect NMR signals from these nuclei. Special attention in *in vivo* MRS is given to the following nuclei: phosphorus (^{31}P), carbon (^{13}C), oxygen (^{17}O), sodium (^{23}Na), and fluorine (^{19}F).

Phosphorus is a main constituent component of high-energy compounds, including ATP synthesized in mitochondria and phosphocreatine (creatine phosphate). Therefore,

Table. Isotopes used in MRS of living organisms, their gyromagnetic ratios, and occurrence under normal conditions.

Nucleus	Gyromagnetic ratio, MHz T^{-1}	Isotope occurrence, %
^{1}H	42.58	99.99
^{13}C	10.71	1.11
^{17}O	−5.77	0.04
^{19}F	40.05	100
^{23}Na	11.26	100
^{31}P	17.24	100

the MRS of phosphorus allows the study of bioenergetic processes in the brain, head, muscles, and other organs [203–205]. Moreover, phosphorus MRS provides other important physiological information, including free magnesium levels, intracellular pH values, and intermediate products of phospholipid metabolism. Carbon MRS is the sole method for the noninvasive observation of neuroenergetic processes and neurotransmitter circulation based on elucidation of the localization of key enzymes and metabolites in neurons and neuroglia [206]. Ongoing studies demonstrate the successful application of the MRS of oxygen nuclei for the investigation of intracellular oxygen metabolism and perfusion in aerobic organs and the measurement of the oxygen metabolism rate and its changes [207]. Recording the NMR response of sodium nuclei by MRS can be used in many areas of clinical and pre-clinical MRI, including stroke diagnostics, characterization of tumor masses (Fig. 16a), the early diagnosis of osteoarthritis, the assessment of articular cartilage conditions, and the evaluation of muscular and renal functions [208–211]. Finally, fluorine is present in living organisms in negligible amounts. On the other hand, fluorine is a valuable component of nontoxic and inert compounds used in a variety of biomedical applications, including anesthetics, contrast media, chemotherapeutic agents, and molecules facilitating dissolution of oxygen carried in artificial blood substitutes [212–214]. Due to this, ^{19}F MRS is a highly efficient noninvasive method for pre-clinical visualization of the distribution of these compounds in the body (Fig. 16b). Also, a signal of fluorine isotopes serves in pre-clinical MRI to visualize the distribution of dual-purpose agents, which can be used either for simultaneous diagnosis and treatment of certain diseases (the so-called theranostics approach) [215] or for novel diagnostics methods employing two or more different diagnostic modalities [216].

A major disadvantage of heteronuclear MRS is its relatively low sensitivity compared with that of hydrogen nuclei MRS due to a variety of factors, including the low concentration of the substances of interest, the rare occurrence of certain isotopes, and the low gyromagnetic ratio of the studied nuclei in comparison with that of hydrogen (see table above). Therefore, transition to ultrahigh magnetic fields appears to be a natural way to improve the sensitivity of heteronuclear MRS. However, strengthening the magnetic field has different consequences for different nuclei, depending on their characteristic relaxation mechanisms [217, 218]. Nevertheless, the overall effect of enhanced sensitivity of heteronuclear MRS is preserved after transition to ultrahigh fields.

Unlike hydrogen MRS employing the same signal source and pipeline as conventional MRI, heteronuclear MRS is only possible with a separate RF signal excitation/receiver circuit and special coils, since the operating frequency in heteronuclear MRS depends on the chosen nucleus. Also, proton decoupling needs to be employed in ^{13}C and ^{31}P MRS

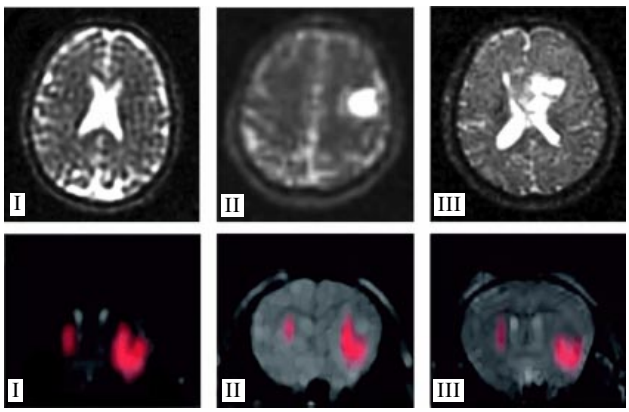

Figure 16. (Color online.) Heteronuclear images acquired in an ultrahigh field. (a) ^{23}Na images in a 7-T field: (I) healthy human brain, (II) cerebral ganglioglioma in the left frontal lobe, and (III) cerebral glioblastoma in the left frontal lobe. (b) Maps showing distribution of ^{19}F-labeled neural stem cells implanted into a mouse (highlighted in pink against the grey background of a classical ^{1}H-image) obtained in a 9.4-T field within (I) 1 hour, (II) 3 days, and (III) 1 week after surgery. The maps allow cell viability to be assayed in the course of time.

to improve both the quality and the resolution of the spectra obtained, because heteronuclear interactions with hydrogen nuclei mediated through electron clouds complicate interpretation of the spectra and broaden resonant lines. Proton decoupling can be achieved by means of RF irradiation of the study tissue at a hydrogen nuclei resonance frequency during detection of a signal from heteronuclei, which results in a greater RF exposure of the studied subject, especially in ultrahigh fields [219]. Moreover, ^{13}C and ^{31}P MRS frequently requires the use of complex magnetization transfer methods to study substances containing these nuclei via recording the signal from hydrogen nuclei. It improves both the sensitivity and specificity of the experiment [220, 221]. For rare ^{13}C isotopes, hyperpolarization techniques allowing an increase in sensitivity by a few orders of magnitude are studied extensively [222]. At present, many technical problems encountered in the creation and preservation of nonequilibrium polarization still confine the application of the MRS of hyperpolarized carbon nuclei to the investigation of fast and dynamic metabolic pathways. At the same time, the method is highly promising for studies in lower fields [223, 224], whereas the use of ultrahigh fields was from the very beginning intended to enhance equilibrium polarization without high-tech hyperpolarization methods. Nowadays, carbon hyperpolarization techniques find wide application in studies using pre-clinical ultrahigh-field scanners [225, 226], e.g., to analyze metabolism in the damaged heart muscle [227, 228] or a neoplasm reaction to angiogenic therapy [229].

Registration of an NMR signal from heteronuclei fails to provide anatomically detailed information due to the low level of studied isotopes or their absence in the body. For this reason, heteronuclear studies are always combined with conventional MRI to ensure correct localization of the heteronuclear signal. A calibration sample is also needed for proper experimental setup and subsequent quantitative analysis [230]. Heteronuclear spectra are characterized by a very wide range of chemical shifts of resonance lines (e.g., 30 ppm for phosphorus and more than 200 ppm for carbon), which leads to serious errors in spatial localization of the source of a heteronuclear MR signal. A peculiar feature of heteronuclear MRS in ultrahigh magnetic fields (together with a high level of technical sophistication, resulting in the increased informative value of the data obtained) is the potential to adapt RF devices initially intended for hydrogen MRS in lower fields due to coincidence of resonance frequencies of rare nuclei in ultrahigh fields and resonance ^{1}H frequency in low fields.

To sum up, heteronuclear MRS is an important complement to traditional MRI, allowing the noninvasive collection of unique physiological and pathological information on the state of living tissue at molecular and cellular levels. Heteronuclear MRS is of special use for studies in ultrahigh fields, since it is free from the problems associated with the creation of efficient RF devices for recording signals from rare nuclei. However, the limited number of ultrahigh field scanners restricts the use of heteronuclear MRS in the human body to specific research programs.

12. Conclusions

The review of human ultrahigh-field MRI features shows that the new tasks specific for technologies that implement static magnetic fields exceeding 3 T give rise to a significant number of new engineering solutions, which possess fundamental scientific and technological novelty. For example, the problem of RF magnetic field inhomogeneity that is induced due to the interference of primary and secondary RF radiation might be solved either with development of new transceiver RF coils that would work in the multi-channel scan mode (moreover, both static and dynamic approach to the channel control might be realized), either by using metamaterials, or dielectric pads, or by switching to the dielectric resonator-based coils, or with a fundamentally novel waveguide MRI technology. Due to the complexity of the new tasks and their interrelationships, integrated solutions appear, and they allow overcoming several barriers on the way to the accessible ultrahigh-field clinical MRI at once. For instance, the use of metamaterials and materials with high permittivity opens opportunities for both reducing the RF load on patients and improving the transmission field homogeneity; the use of MR fingerprinting and compressed sensing technique also contributes to this aim. The latter methods allow significant reduction of the scanning time due to the limited data acquisition.

On the other hand, the new opportunities of ultrahigh field MRI substantially expand the range of its applications. The improved spatial and functional resolution of fMRI makes it possible to observe the brain structures that formerly have been accessible only with invasive methods. The increased efficiency of magnetization transfer leads to the development of more effective disease diagnostic methods. Heteronuclear MRI also increases the number of diagnostic tasks that can be solved by MRI; moreover, it allows studying metabolic processes *in vivo*. The fingerprint recognition facilitates transition from qualitative to quantitative assessment of MR images, which, in turn, improves the efficiency of clinical diagnostics. Such technologies most often undergo preliminary tests in pre-clinical ultrahigh-field MR scanners that are not intended for human scanning. For this reason, a large part of modern studies in this field that has not yet been tested on humans (or tested in MRI scanners that allow human body scanning, at least) is not included in this review. Such research and technologies include magnetization trans-

fer experiments conducted at the Institute of Cytology and Genetics, Siberian Branch of the Russian Academy of Sciences [231–233], heteronuclear applied research at Lomonosov Moscow State University [234–236], and certain aspects of the use of new contrast agents described in the works of the team of the Pirogov Russian National Research Medical University [237–240].

This review on ultrahigh field human MRI clearly shows that although this diagnostics method is not clinically implemented yet, intensive works intended to overcome existing technical constraints are carried out throughout the world, and the search for new diagnostic opportunities for modern medicine provided by ultrahigh magnetic fields is in progress.

Acknowledgements

The work on the use of metamaterials and dielectric structures in MRI was supported by the Ministry of Science and Higher Education of the Russian Federation (project no. 3.2465.2017/PCh). Part of the work (Section 5) was performed with the financial support of the country's leading universities in the framework of the ITMO University Fellowship and Professorship Program. The work reported in Sections 6–9 was supported by the Russian Science Foundation (project no. 18-75-10088).

References

1. MacWilliams B *Nature* **426** 375 (2003)
2. Lauterbur P C *Nature* **242** 190 (1973)
3. Chang K J et al. *RadioGraphics* **28** 1983 (2008)
4. Carr J C et al. *Radiology* **219** 828 (2001)
5. Rajiah P, Bolen M A *RadioGraphics* **34** 1612 (2014)
6. Grade M et al. *Neuroradiology* **57** 1181 (2015)
7. Ulmer S, Jansen O (Eds) *fMRI. Basics and Clinical Applications* (Dordrecht: Springer, 2013)
8. Fountas K (Ed.) *Novel Frontiers of Advanced Neuroimaging* (London: InTech, 2013)
9. Le Bihan D *Nature Rev. Neurosci.* **4** 469 (2003)
10. Delorme S, Weber M-A *Cancer Imaging* **6** 95 (2006)
11. Oberhaensli R D et al. *Br. J. Radiol.* **59** 695 (1986)
12. Cadoux-Hudson T A D et al. *Br. J. Cancer* **60** 430 (1989)
13. Stankovic Z et al. *Cardiovasc. Diagn. Ther.* **4** 173 (2014)
14. Burstein D, Bashir A, Gray M L *Invest. Radiol.* **35** 622 (2000)
15. Wattjes M P, Barkhof F *Eur. Radiol.* **22** 2304 (2012)
16. Hoult D I, Bhakar B *Concepts Magn. Reson.* **9** 277 (1997)
17. Chizhik V I et al. *Magnetic Resonance and Its Applications* (Cham: Springer, 2014)
18. Bottomley P A et al. *Med. Phys.* **11** 425 (1984)
19. Dietrich O et al. *Eur. J. Radiol.* **65** 29 (2008)
20. Kraff O, Quick H H *J. Magn. Reson. Imaging* **46** 1573 (2017)
21. Moser E et al. *NMR Biomed.* **25** 695 (2012)
22. van der Zwaag W et al. *NMR Biomed.* **29** 1274 (2016)
23. Stüber C et al. *NeuroImage* **93** 95 (2014)
24. Marques J P et al. *NeuroImage* **49** 1271 (2010)
25. Van de Moortele P-F et al. *NeuroImage* **46** 432 (2009)
26. Visser F et al. *Magn. Reson. Med.* **64** 194 (2010)
27. Kangarlu A et al. *Magn. Reson. Mater. Phys. Biol. Med.* **9** 81 (1999)
28. Grams A E et al. *Clin. Neuroradiol.* **23** 17 (2013)
29. Hayes C E et al. *J. Magn. Reson. 1969* **63** 622 (1985)
30. Vaughan J T et al. *Magn. Reson. Med.* **32** 206 (1994)
31. Gabriel S et al. *Phys. Med. Biol.* **41** 2271 (1996)
32. Collins C M et al. *J. Magn. Reson. Imaging* **21** 192 (2005)
33. Ibrahim T S et al. *Magn. Reson. Imaging* **19** 219 (2001)
34. Deniz C M et al. *Magn. Reson. Med.* **69** 1379 (2013)
35. van den Bergen B et al. *J. Magn. Reson. Imaging* **30** 194 (2009)
36. Brink W M et al. *J. Magn. Reson. Imaging* **42** 855 (2015)
37. Katscher U, Börnert P *NMR Biomed.* **19** 393 (2006)
38. Avdievich N I *Appl. Magn. Reson.* **41** 483 (2011)
39. Adriany G et al. *Magn. Reson. Med.* **63** 1478 (2010)
40. Raaijmakers A J E et al. *Magn. Reson. Med.* **75** 1366 (2016)
41. Shajan G et al. *Magn. Reson. Med.* **71** 870 (2014)
42. Ertürk M A et al. *Magn. Reson. Med.* **77** 884 (2017)
43. Roemer P B et al. *Magn. Reson. Med.* **16** 192 (1990)
44. Keil B et al. *Magn. Reson. Med.* **66** 1777 (2011)
45. von Morze C et al. *Concepts Magn. Reson. B* **31** 37 (2007)
46. Avdievich N I et al. *NMR Biomed.* **26** 1547 (2013)
47. Yan X et al. *Appl. Magn. Reson.* **46** 59 (2015)
48. Hurshkainen A A et al. *J. Magn. Reson.* **269** 87 (2016)
49. Sievenpiper D et al. *IEEE Trans. Microwave Theory Tech.* **47** 2059 (1999)
50. Padormo F et al. *NMR Biomed.* **29** 1145 (2016)
51. Curtis A T et al. *Magn. Reson. Med.* **68** 1109 (2012)
52. Gilbert K M et al. *NMR Biomed.* **24** 815 (2011)
53. Hess A T et al. *Magn. Reson. Med.* **73** 1864 (2015)
54. Snyder C J et al. *Magn. Reson. Med.* **61** 517 (2009)
55. Rodgers C T et al. *Magn. Reson. Med.* **70** 1038 (2013)
56. Vaughan J T et al. *Magn. Reson. Med.* **61** 244 (2009)
57. Chang G et al. *J. Magn. Reson. Imaging* **39** 1384 (2014)
58. Brown R et al. *Invest. Radiol.* **49** 35 (2014)
59. van den Bergen B et al. *NMR Biomed.* **24** 358 (2011)
60. Fischer A et al. *PLoS ONE* **9** e97465 (2014)
61. Setsompop K et al. *Magn. Reson. Med.* **60** 1422 (2008)
62. Schmitter S et al. *Invest. Radiol.* **49** 314 (2014)
63. Schmitter S et al. *Magn. Reson. Med.* **70** 1210 (2013)
64. Wu X et al. *Quant. Imaging Med. Surg.* **4** 4 (2014)
65. Wiggins G C et al. *Magn. Reson. Med.* **56** 216 (2006)
66. Engheta N, Ziolkowski R W (Eds) *Metamaterials: Physics and Engineering Explorations* (Hoboken, N.J.: Wiley-Interscience, 2006)
67. Gorkunov M V, Lapine M V, Tretyakov S A *Crystallogr. Rep.* **51** 1048 (2006); *Kristallografiya* **51** 1117 (2006)
68. Lapine M, Tretyakov S *IET Microwaves Antennas Propag.* **1** 3 (2007)
69. Kildishev A V, Shalaev V M *Phys. Usp.* **54** 53 (2011); *Usp. Fiz. Nauk* **181** 59 (2011)
70. Vendik I B, Vendik O G *Tech. Phys.* **58** 1 (2013); *Zh. Tekh. Fiz.* **83** (1) 3 (2013)
71. Veselago V G *Phys. Usp.* **46** 764 (2003); *Usp. Fiz. Nauk* **173** 790 (2003)
72. Wiltshire M C K et al. *Science* **291** 849 (2001)
73. Radu X, Garray D, Craeye C *Metamaterials* **3** 90 (2009)
74. Freire M J et al. *J. Magn. Reson.* **203** 81 (2010)
75. Glybovski S B et al. *Phys. Rep.* **634** 1 (2016)
76. Remnev M A, Klimov V V *Phys. Usp.* **61** 157 (2018); *Usp. Fiz. Nauk* **188** 169 (2018)
77. Slobozhanyuk A P et al. *Adv. Mater.* **28** 1832 (2016)
78. Shchelokova A V et al. *J. Magn. Reson.* **286** 78 (2018)
79. Shchelokova A V et al. *Phys. Rev. Appl.* **9** 014020 (2018)
80. Schmidt R et al. *Sci. Rep.* **7** 1678 (2017)
81. Schmidt R, Webb A *ACS Appl. Mater. Interfaces* **9** 34618 (2017)
82. Jouvaud C et al. *Appl. Phys. Lett.* **108** 023503 (2016)
83. Zubkov M et al. *NMR Biomed.* **31** e3952 (2018)
84. Hurshkainen A et al. *Sci. Rep.* **8** 9190 (2018)
85. Simovski C R et al. *Adv. Mater.* **24** 4229 (2012)
86. Lapine M, Shadrivov I V, Kivshar Yu S *Rev. Mod. Phys.* **86** 1093 (2014)
87. Boardman A D et al. *Laser Photon. Rev.* **5** 287 (2011)
88. Lapine M *Phys. Status Solidi B* **254** 1600462 (2017)
89. Webb A G *Concepts Magn. Reson. A* **38** 148 (2011)
90. Yang Q X et al. *J. Magn. Reson. Imaging* **24** 197 (2006)
91. Teeuwisse W M et al. *Magn. Reson. Med.* **67** 912 (2012)
92. O'Reilly T P A, Webb A G, Brink W M *J. Magn. Reson.* **270** 108 (2016)
93. Yu Z et al. *Magn. Reson. Med.* **78** 383 (2017)
94. Aussenhofer S A, Webb A G *Magn. Reson. Med.* **68** 1325 (2012)
95. Aussenhofer S A, Webb A G *J. Magn. Reson.* **243** 122 (2014)

96. Schmidt R, Teeuwisse W, Webb A *Magn. Reson. Med.* **77** 2431 (2017)
97. Vaughan J T et al. *Magn. Reson. Med.* **52** 851 (2004)
98. Brunner D O et al. *Nature* **457** 994 (2009)
99. Schneider H J, Dullenkopf P *Rev. Sci. Instrum.* **48** 68 (1977)
100. Andreychenko A et al. *Magn. Reson. Med.* **70** 875 (2013)
101. Andreychenko A et al. *Magn. Reson. Med.* **70** 885 (2013)
102. Brunner D O et al. *Magn. Reson. Med.* **66** 290 (2011)
103. Andreychenko A et al. *Magn. Reson. Med.* **71** 1641 (2014)
104. Andreychenko A et al., in *Proc. of the 18th Annual Meeting, International Society for Magnetic Resonance in Medicine ISMRM, Stockholm, Sweden 1–7 May 2010* (Stockholm: ISMRM, 2010)
105. Andreychenko A et al., in *Proc. of the 21st Annual Meeting, International Society for Magnetic Resonance in Medicine ISMRM, Salt Lake City, Utah, USA, 20–26 April 2013* (Salt Lake City: ISMRM, 2013)
106. Redpath T W *Br. J. Radiol.* **71** 704 (1998)
107. Glover G H *Neurosurg. Clin. North Am.* **22** 133 (2011)
108. Vaughan J T et al. *Magn. Reson. Med.* **46** 24 (2001)
109. Guérin B et al. *Magn. Reson. Med.* **78** 1969 (2017)
110. Pfrommer A, Henning A *Magn. Reson. Med.* **80** 2122 (2018)
111. Pohmann R, Speck O, Scheffler K *Magn. Reson. Med.* **75** 801 (2016)
112. Hoogenraad F G C et al. *Magn. Reson. Imaging* **18** 405 (2000)
113. Lutti A et al. *Magn. Reson. Med.* **69** 1657 (2013)
114. Olman C A, Yacoub E *Open Neuroimag. J.* **5** 74 (2011)
115. Duong T Q et al. *Magn. Reson. Med.* **48** 589 (2002)
116. Norris D G *NeuroImage* **62** 1109 (2012)
117. Bandettini P A et al. *Magn. Reson. Med.* **25** 390 (1992)
118. Uludağ K, Müller-Bierl B, Uğurbil K *NeuroImage* **48** 150 (2009)
119. Wedeen W J et al. *Magn. Reson. Med.* **54** 1377 (2005)
120. Tuch D S et al. *Magn. Reson. Med.* **48** 577 (2002)
121. Tuch D S *Magn. Reson. Med.* **52** 1358 (2004)
122. Uğurbil K et al. *NeuroImage* **80** 80 (2013)
123. Huisman T A G M et al. *Eur. Radiol.* **16** 1651 (2006)
124. Chung A W et al. *Magn. Reson. Imaging* **31** 742 (2013)
125. Choi S et al. *Magn. Reson. Imaging* **29** 739 (2011)
126. Guilfoyle D N et al. *NMR Biomed.* **16** 468 (2003)
127. Mukherjee P et al. *Magn. Reson. Imaging* **26** 171 (2008)
128. Sigmund E E, Gutman D *Magn. Reson. Imaging* **29** 752 (2011)
129. Strotmann B et al. *J. Magn. Reson. Imaging* **39** 1018 (2014)
130. Vu A T et al. *NeuroImage* **122** 318 (2015)
131. Johnson G A et al. *J. Comp. Neurol.* **527** 2146 (2019)
132. Wang N et al. *Brain Struct. Funct.* **223** 4323 (2018)
133. Yamasaki T et al. *Magn. Reson. Imaging* **33** 95 (2015)
134. Shultz S R et al. *J. Cereb. Blood Flow Metab.* **35** 1339 (2015)
135. Laitinen T et al. *Front. Neurosci.* **9** 128 (2015)
136. Webster K M et al. *J. Neuroinflammat.* **12** 238 (2015)
137. Kelm N D et al. *NeuroImage* **124** 612 (2016)
138. Hammelrath L et al. *NeuroImage* **125** 144 (2016)
139. Liu G et al. *NMR Biomed.* **26** 810 (2013)
140. van Zijl P C M, Yadav N N *Magn. Reson. Med.* **65** 927 (2011)
141. Rivlin M et al. *Sci. Rep.* **3** 3045 (2013)
142. Rivlin M, Navon G *Sci. Rep.* **6** 32648 (2016)
143. Walker-Samuel S et al. *Nature Med.* **19** 1067 (2013)
144. Cai K et al. *Nature Med.* **18** 302 (2012)
145. Schmitt B et al. *Radiology* **260** 257 (2011)
146. Wu B et al. *EJNMMI Phys.* **3** 19 (2016)
147. Harris R J et al. *Neuro-Oncol.* **17** 1514 (2015)
148. Song X et al. *Nature Commun.* **6** 6719 (2015)
149. Chen L Q et al. *Mol. Imaging Biol.* **17** 488 (2015)
150. Moon B F et al. *Contrast Media Mol. Imaging* **10** 446 (2015)
151. Yang X et al. *Contrast Media Mol. Imaging* **11** 304 (2016)
152. Wu Y et al. *Magn. Reson. Med.* **75** 2432 (2016)
153. Zhang X-Y et al. *Magn. Reson. Imaging* **34** 1100 (2016)
154. Wells J A et al. *NeuroImage* **111** 369 (2015)
155. Goerke S et al. *NMR Biomed.* **28** 906 (2015)
156. Pépin J et al. *NeuroImage* **139** 53 (2016)
157. Sekhar A et al. *Proc. Natl. Acad. Sci. USA* **113** E6939 (2016)
158. Wang F et al. *Magn. Reson. Med.* **76** 1531 (2016)
159. Qaisar S et al. *J. Commun. Networks* **15** 443 (2013)
160. Lustig M, Donoho D, Pauly J M *Magn. Reson. Med.* **58** 1182 (2007)
161. Rosenkrantz A B et al. *J. Magn. Reson. Imaging* **41** 1365 (2015)
162. Smith D S et al. *Phys. Med. Biol.* **56** 4933 (2011)
163. Onishi N et al. *J. Magn. Reson. Imaging* **47** 97 (2018)
164. Ono A et al. *Magn. Reson. Imaging* **43** 42 (2017)
165. Yamamoto T et al. *PLoS ONE* **13** e0189493 (2018)
166. Moghari M H et al. *Magn. Reson. Med.* **79** 761 (2018)
167. Feng L et al. *J. Magn. Reson. Imaging* **45** 966 (2017)
168. Menzel M I et al. *Magn. Reson. Med.* **66** 1226 (2011)
169. Bhave S et al. *Magn. Reson. Med.* **75** 1175 (2016)
170. Park C-A et al. *Appl. Magn. Reson.* **46** 1189 (2015)
171. Cho Z-H et al. *J. Neurol.* **260** 144 (2013)
172. Lee Y-B et al. *Vascular Med.* **18** 314 (2013)
173. Milles J et al., in *Proc. of the 10th IEEE Intern. EMBS Conf. Information Technology Applications in Biomedicine, ITAB, 2010* (Piscataway, NJ: IEEE, 2010)
174. Yarach U et al. *Magn. Reson. Med.* **78** 2250 (2017)
175. Madelin G et al. *J. Magn. Reson.* **214** 360 (2012)
176. Gnahm C, Nagel A M *NeuroImage* **105** 452 (2015)
177. Fang Z et al. *Magn. Reson. Med.* **76** 440 (2016)
178. Paulsen J, Bajaj V S, Pines A *J. Magn. Reson.* **205** 196 (2010)
179. Zhang J et al. *Magn. Reson. Med.* **81** 140 (2019)
180. Bai R et al. *J. Magn. Reson.* **255** 88 (2015)
181. Maguire M L et al. *J. Cardiovasc. Magn. Reson.* **17** 45 (2015)
182. Stejskal E O, Tanner J E *J. Chem. Phys.* **42** 288 (1965)
183. Tanner J E *J. Chem. Phys.* **52** 2523 (1970)
184. Vold R L et al. *J. Chem. Phys.* **48** 3831 (1968)
185. Markley J L, Horsley W J, Klein M P *J. Chem. Phys.* **55** 3604 (1971)
186. Carr H Y, Purcell E M *Phys. Rev.* **94** 630 (1954)
187. Ma D et al. *Nature* **495** 187 (2013)
188. McGivney D F et al. *IEEE Trans. Med. Imaging* **33** 2311 (2014)
189. Cauley S F et al. *Magn. Reson. Med.* **74** 523 (2015)
190. Doneva M et al. *Magn. Reson. Med.* **64** 1114 (2010)
191. Lattanzi R et al. *Magn. Reson. Imaging* **49** 32 (2018)
192. Zhang X et al. *Magn. Reson. Imaging* **41** 53 (2017)
193. Hoppe E et al. *Stud. Health Technol. Inform.* **243** 202 (2017)
194. Badve C et al. *Am. J. Neuroradiol.* **38** 492 (2017)
195. Koolstra K et al. *Magn. Reson. Med.* **81** 2551 (2019)
196. Chen Y et al. *Radiology* **279** 278 (2016)
197. Hamilton J I et al. *Magn. Reson. Med.* **77** 1446 (2017)
198. Yu A C et al. *Radiology* **283** 729 (2017)
199. Gao Y et al. *NMR Biomed.* **28** 384 (2015)
200. Buonincontri G, Sawiak S J *Magn. Reson. Med.* **76** 1127 (2016)
201. Stara R et al. *Appl. Magn. Reson.* **48** 307 (2017)
202. Cloos M A et al. *Nature Commun.* **7** 12445 (2016)
203. Argov Z, Bank W J *Ann. Neurol.* **30** 90 (1991)
204. Valkovič L, Chmelík M, Krššák M *Anal. Biochem.* **529** 193 (2017)
205. Larson-Meyer D E et al. *NMR Biomed.* **13** 14 (2000)
206. Rothman D L et al. *NMR Biomed.* **24** 943 (2011)
207. Zhu X-H, Chen W *Analyt. Biochem.* **529** 171 (2017)
208. Madelin G et al. *Prog. Nucl. Magn. Reson. Spectrosc.* **79** 14 (2014)
209. Nagel A M et al. *Invest. Radiol.* **46** 539 (2011)
210. Nagel A M et al. *NMR Biomed.* **29** 759 (2016)
211. Lee K-C et al. *J. Med. Biol. Eng.* **35** 643 (2015)
212. Ruiz-Cabello J et al. *NMR Biomed.* **24** 114 (2011)
213. Ruiz-Cabello J et al. *Magn. Reson. Med.* **60** 1506 (2008)
214. Temme S et al. *Circulation* **131** 1405 (2015)
215. Shin S H et al. *Theranostics* **7** 562 (2017)
216. Wang Z et al. *Adv. Healthcare Mater.* **3** 1326 (2014)
217. Qiao H et al. *Magn. Reson. Imaging* **24** 1281 (2006)
218. Zhu X-H et al. *Magn. Reson. Med.* **45** 543 (2001)
219. Li N, Li S, Shen J *Front. Phys.* **5** 26 (2017)
220. Lagemaat M W et al. *NMR Biomed.* **29** 256 (2016)
221. Henry P-G, Tkáč I, Gruetter R *Magn. Reson. Med.* **50** 684 (2003)
222. Ardenkjær-Larsen J H et al. *Proc. Natl. Acad. Sci. USA* **100** 10158 (2003)
223. Nelson S J et al. *Sci. Transl. Med.* **5** 198ra108 (2013)
224. Eldirdiri A et al. *Tomography* **4** 110 (2018)

225. DeVience S J et al. *Sci. Rep.* **7** 1907 (2017)
226. Schmidt A B et al. *PLoS ONE* **13** e0200141 (2018)
227. Dodd M S et al. *Circ. Cardiovasc. Imaging* **7** 895 (2014)
228. Oh-Ici D et al. *Radiology* **278** 742 (2016)
229. Matsumoto S et al. *Antioxid. Redox Signal.* **21** 1145 (2014)
230. van Gorp J S et al. *NMR Biomed.* **28** 1433 (2015)
231. Khodanovich M Yu et al. *Sci. Rep.* **7** 46686 (2017)
232. Naumova A V et al. *NeuroImage* **147** 985 (2017)
233. Khodanovich M Yu et al. *J. Cereb. Blood Flow Metab.* **38** 919 (2018)
234. Anisimov N et al. *J. Phys. Conf. Ser.* **886** 012001 (2017)
235. Gervits L L et al. *BioNanoScience* **7** 456 (2017)
236. Volkov D V et al. *Appl. Magn. Reson.* **49** 71 (2018)
237. Namestnikova D et al. *PLoS ONE* **12** e0186717 (2017)
238. Abakumova T et al. *Contrast Media Mol. Imaging* **11** 15 (2016)
239. Semkina A S et al. *Bull. Exp. Biol. Med.* **161** 292 (2016); *Byull. Eksp. Biol. Med.* **161** 256 (2016)
240. Semkina A S et al. *Bull. Exp. Biol. Med.* **162** 808 (2017); *Byull. Eksp. Biol. Med.* **162** 781 (2016)